

Vibration enhanced cell growth induced by surface acoustic waves as *in vitro* wound healing model

Manuel S. Brugger^{1,2}, Kathrin Baumgartner^{1,3}, Sophie C. F. Mauritz¹, Stefan C. Gerlach^{1,4}, Florian Röder¹, Christine Schlosser⁵, Regina Fluhrer^{5,6}, Achim Wixforth^{1,8} and Christoph Westerhausen^{1,7,8}

¹Experimental Physics I, Institute of Physics, University of Augsburg, Universitätsstraße 1, 86159 Augsburg, Germany

²Stiftung der Deutschen Wirtschaft (sdw) gGmbH, Breite Straße 29, 10178 Berlin, Germany

³Studienstiftung des deutschen Volkes e.V., Ahrstraße 41, 53175 Bonn, Germany

⁴Hans-Seidel-Stiftung e.V., Lazarettstraße 33, 80636 München, Germany

⁵Biochemistry and Molecular Biology, Institute of Theoretical Medicine, University of Augsburg, Universitätsstraße 2, 86159 Augsburg, Germany

⁶DZNE – German Center for Neurodegenerative Diseases, Feodor-Lynen-Str 17, 81377 Munich, Germany

⁷Physiology, Institute of Theoretical Medicine, University of Augsburg, Universitätsstraße 2, 86159 Augsburg, Germany

⁸Center for NanoScience (CeNS), Schellingstraße 4, 80799 Munich, Germany

Corresponding Author:

Christoph Westerhausen

University of Augsburg, Institute of Theoretical Medicine, Universitätstr. 2, 86159 Augsburg

Tel.: +049-821-598 3311

christoph.westerhausen@gmail.com

M.S.B., A.W. and C.W. designed the study; M.S.B., K.R., S.C.F.M., S.C.G., F.R., C.S. and R.F. performed experiments and analyzed data; and M.S.B. and C.W. wrote the manuscript.

Abstract

We report on *in vitro* wound-healing and cell growth studies under the influence of radio frequency cell stimuli. These stimuli are supplied either by piezoactive Surface Acoustic Waves (SAW) or by micro electrode generated electric fields, both at frequencies around 100 MHz. Employing live cell imaging, we studied the time and power dependent healing of artificial wounds on a piezoelectric chip for different cell lines. If the cell stimulation is mediated by piezomechanical Surface Acoustic Waves, we observe a pronounced, significant maximum of the cell growth rate at a specific SAW amplitude resulting in an increase of the wound-healing speed of up to $135 \pm 85\%$ as compared to an internal reference. In contrast, cells being stimulated only by electrical fields of the same magnitude as the ones exposed to SAW, exhibit no significant effect. In this study, we investigate this effect for different wavelengths, amplitude modulation of the applied electrical radio frequency (rf)-signal and different wave modes. Furthermore, to obtain insight on the biological response to the stimulus, we also determined both the cell proliferation rate and the cellular stress levels. While the proliferation rate is significantly increased for a wide power range, cell stress remains low and within the normal range. Our findings demonstrate that SAW-based vibrational cell stimulation bears the potential for an alternative method to conventional ultra sound treatment overcoming some of its limitations.

surface acoustic waves | vibration | cell growth | migration | stimulation | wound-healing assay | proliferation | reactive oxygen species

Significance

Ultrasonic pressure fields have been proven to be beneficial for cell growth *in vitro* and in patients. However, conventional therapeutic ultrasound treatment is subjected to limitations such as time restriction, external application or energy loss. The application of Surface Acoustic Waves (SAW) can help to overcome some drawbacks. To understand the underlying mechanism, the adjusting parameters of SAW and the intracellular response on the stimulation are evaluated. We identified a dependence of cell growth on SAW-intensity and the presence of a vertical substrate deflection. While

the cellular stress (reactive oxygen species) remains in the normal range, both cell migration and proliferation are increased. Due to the experimental design, the effect of enhanced cell growth is dominated by increased cell migration.

Introduction

Currently, improving and acceleration of wound-healing is of highest interest in medical science. Reports of 'smart' wound-healing techniques range from on-demand emission of inflammatory inhibiting materials¹ to increased cell growth by releasing growth factors upon cell induced traction forces². There have been also reports on techniques including active electrical and mechanical cell stimulation, *e.g.* by using soundwaves. Already in the 1960s, Knoch and Klug proposed the use of therapeutic ultrasound (US)^{3,4}. Since then, it has been shown that US can in fact improve the regeneration and healing rate of soft and hard tissue up to 40 %⁵⁻⁷ for spatially distributed intensities between $I_{US} = 30 \text{ mW/cm}^2$ to $I_{US} = 500 \text{ mW/cm}^2$ ^{8,9}. Furthermore, the potential of US treatment to stimulate the spleen in order to treat inflammatory diseases has been recently demonstrated¹⁰. Despite the obviously beneficial effects of therapeutic US, the application of the technique is still subject to restrictions. It turns out, for example, that the beneficial effects of US undergo a turnaround leading to a suppressed fracture healing if the US intensity applied is higher than $I_{US} = 1 \text{ W/cm}^2$ ¹¹. In this context, it has been shown that US application may induce a temperature rise in tissue of about 0.86 K/min at a power of 1 W/cm^2 and a frequency of 1 MHz¹², limiting the US therapy to short pulses and low intensities of about $I = 30 \text{ mW/cm}^2$ ¹³. Moreover, high costs and the requirement of medical assistance during US exposure impede a long-term treatment and limit the application to single sessions. As an answer to these limitations, we recently proposed a novel approach employing surface acoustic waves (SAW) for tissue healing and recovery treatment to overcome some disadvantages of the US-based methods¹⁴. In recent years, SAW can be found as mass products in, *e.g.*, filters and rf signal processing devices in mobile phones, and high frequency applications but also for the active acoustic manipulation in microfluidic applications. Based on the effect of acoustic streaming¹⁵, SAW have recently become a quite unique tool in biomedical applications for cell manipulation¹⁶, deadhesion under flow¹⁷ or on-demand patterning¹⁸. Moreover, first results show that SAW-based biochips can yield in tailored standing wave body force fields which bear the fascinating potential to create a well-defined neural network on a chip¹⁹. In a recent report on SAW-assisted *in vitro* wound-healing, we were able to demonstrate positive stimulation of cell growth up to $15.2 \pm 1.7 \%$. After carefully excluding parasitic temperature, ballistic or nutrient induced stimulation effects, we were able to narrow down the beneficial SAW-induced mechanisms to the mechanical and electrical component of the SAW. Our findings were later confirmed and supported by Greco et al. who investigated the impact of SAW on cell proliferation²⁰.

In this manuscript, we continue on the impact of SAW-stimulation on cell growth, narrow down the stimulation mechanism, identify the most relevant adjusting parameters and provide insights into the intracellular reactions induced by SAW. Moreover, we also address the question whether the observed phenomenon is due to cell migration or proliferation.

Methods and Materials

If not stated otherwise, *in vitro* wound-healing assays were performed while measuring cellular parameters for three cell lines, 'Madine-Darby Canine Kidney' (MDCK-II) and human osteosarcoma 'sarcoma osteogenic' (SaOs-2) and 'Human embryonic kidney' (T-REx™-293). For detailed information see SI.

The experimental setup

A SAW-chip is a piezoelectric chip with micron sized metal electrodes, so-called Interdigital Transducers (IDT) consisting of two multi-finger electrodes²¹. An rf-signal of power P_{IN} and frequency f_{res} is converted into an acoustic wave with a width of the transducer and a wavelength of λ_{SAW} . Dependent on the substrate, cut and transducer design the wave is either a Rayleigh SAW for LiNbO_3 rotated around the X-axis by 128° (128° rot Y-cut) or a love wave for LiTaO_3 (40° rot X-Y-cut)²². To ensure biocompatibility and to protect the electrodes, the whole chip except for the contact pads is covered with a SiO_2 layer.

Due to the IDTs bidirectionality (3dB) as well as based on years of experience with SAW with various other, small insertion loss mechanisms, we conservatively estimated P_{SAW} of the propagating wave as $P_{SAW} \approx \frac{1}{4} P_{IN}$. The SAW causes acoustic streaming²³ with a $1/e$ -decay length of the SAW-intensity in propagation-direction of $l_{opX}^{Calc} = 12.5\lambda_{SAW} = 331 \mu\text{m}$ ²⁴. Considering l_{opX}^{Calc} , P_{SAW} and W , the SAW-intensity, I_{SAW} acting upon the cells is approximately²⁴:

$$I_{SAW} = P_{SAW} \frac{\left(1 - \frac{1}{e}\right)}{W l_{opX}^{Calc}} \approx 80 \frac{\text{mW}}{\text{cm}^2} \text{ for } P_{IN} = 1 \text{ mW and } I_{SAW} \approx 1 \frac{\text{W}}{\text{cm}^2} \text{ for } P_{IN} = 13.6 \text{ mW.}$$

The SAW-chip was mounted on a sample holder (Fig. 1 a-2)). A polydimethylsiloxane (PDMS) chamber ($V = 3 \text{ ml}$) (Sylgard 184 Silicone Elastomer, Dow corning, Germany) was placed on top of the SAW-chip (Fig. 1 a-1)). The culture insert (CI) (Ibidi® GmbH, Martinsried, Germany; width $500 \pm 50 \mu\text{m}$) was placed with its gap oriented parallel to and about $d = 50 \mu\text{m}$ away from the IDT (Fig. 1 a-3)). 80.000 cells were seeded into each chamber and cultivated to reach confluency. After removal of the CI the cell migration into the cell-free area was recorded in phase contrast images every 5 min with a 10 x objective. The SAW-chips were connected to a rf-generator (SML 01, Rhode & Schwarz, Munich, Germany) with an amplifier (gain $G = 30 \text{ dB}$, AMP590033H-T, Becker Nachrichtentechnik GmbH, Asbach, Germany).

Characterization of the resulting flow field

We determined the effective flow field $25 \mu\text{m}$ above the surface using scanning particle image velocimetry (sPIV) as reported earlier²⁵ by scanning an area larger than a single field of view and combining the multiple micro-particle image velocimetry measurements to a single velocity field.

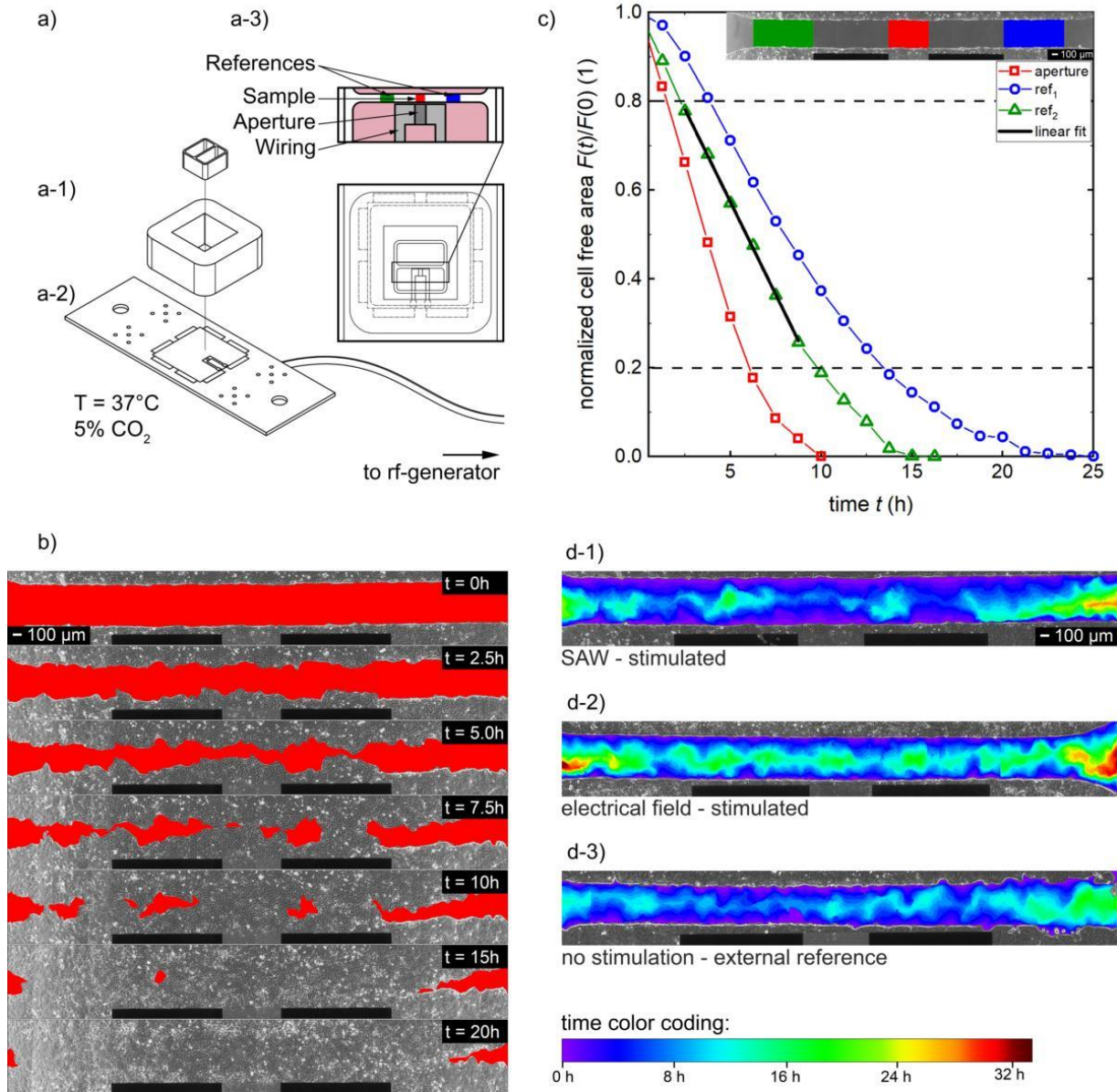


Figure 1: Sketch of the experimental setup and concept of the data analysis. a) Technical drawing of the setup. A culture insert was used to produce a standardized artificial wound in a confluent cell layer (pink) of MDCK-II cells in front of the IDT aperture. b) Time sequenced images of the progressive cell migration of MDCK-II cells into the cell-free area (red). c) Time dependent shrinkage of the normalized cell-free area in the regions of interest (red: stimulated section, green/blue: internal reference). The section between $0.8 < F(t)/F(0) < 0.2$ is approximated by a linear fit. The slope gives the surface area migration rate A_{mig} . d) Superimposed snapshots of the cell fronts of single experiments at different time steps with a time dependent color coded migration progress. d-1)-2) Analyzable samples. d-3) Cell layer quality of the right area does not meet the requirements.

Measuring intracellular parameters

To understand the cellular response and the biochemical processes, we determined the production of ROS, the proliferation rate and their internal and external reference following standard protocols (see SI for details).

Data analysis

Wound-Healing Assays:

Fig. 1 b) shows a chronological sequence of a typical experiment with MDCK-II cells at different time points. The cell fronts continuously invade the red-labelled cell-free area. Based on previous experiments, we know that the width of the sound path is strictly limited to the size of the aperture²⁶. Therefore, only cells in front and rear of the aperture are directly stimulated by SAW. The cell-free area in this region is called *aperture* in the following. As shown in the inset of Fig. 1. c) the internal references indicated in green and blue are located next to the wiring. At these positions, there is sufficient distance that SAW does not interact with the cells. Yet, cells grow under identical conditions (i.e. nutrient supply, temperature, cell density, cell cycle, viability etc.) as in front of the aperture.

The 'surface area migration rate A_{mig} ', describes the speed of cell migration and growth into the free space. The cell-free area is determined for every region of interest in $\Delta t = 1.25$ h intervals and plotted as function of the time in Fig. 1. c) normalized to $F(0)$ and approximated by a linear fit. To exclude artefacts, like delay time due to cellular polarization in the beginning or non-uniform surface-coverage before reaching confluency, only values in the interval $0.8 < F(t) < 0.2$ are fitted linearly²⁷ resulting in A_{mig} with the unit area loss in percent per hour. To compare the results and to avoid culture dependent influences, the aperture $A_{\text{mig, aperture}}$ is divided by the mean of the internal references $A_{\text{mig, int. ref.}}$ and defined as stimulation efficacy $E := A_{\text{mig, aperture}}/A_{\text{mig, int. ref.}}$ (Fig. 2 d). For each power four separate experiments are performed if not indicated otherwise.

Superimposed composition to the complete sequence of one sample allow identifying the cell migration over time in one color coded image as shown in Fig. 1 d). Dependent on the elapsed time, the rainbow-color changes from purple to deep red (early coverage results in blue tones). An exemplary development of a superimposed image as a result of the temporal evolution of the cell migration can be found in the SI. To maintain a high-quality content of the data, the cell layer in the analyzed region must meet specific demands like confluency, cell density and viability. As exemplary shown in Fig. 1 d-3) the right part of the cell layer was not completely confluent as compared to the one in Fig. 1 d-1) - 2). Therefore, only the left part was considered for the internal reference. However, this concerns only a small fraction of all samples.

The variation of the speed of coverage of the cell free area along this artificial wound is studied in more detail in the SI.

Fluorescence images:

To evaluate fluorescence images, the data were analyzed using a self-developed software in MATLAB (MathWorks, Natick, MA, USA) as described in detail in the SI.

Results and Discussion

A previous study showed successful stimulation of SaOs-2 cells for continuous stimulation with Rayleigh modes of wave length $\lambda=25$ μm in the power range of $P_{\text{IN}} = 4$ mW to 8 mW. The structure of the study presented here is as follows:

First, based on our previously reported findings, we vary the wave length, wave mode and the duty cycle of the stimulation to identify the most relevant SAW parameters to answer the questions: i) Does an increase of λ further enhance the effect?, ii) Do shear waves also result in a significant effect?, iii) Do pulsed Rayleigh waves also result in enhanced wound healing on a chip?

Secondly, we can positively state that the effect is conserved for other cell lines and collective cell migration. We in-depth elucidate the dependence of the effect on the applied power level. Third, to further identify the intracellular response, we quantify reactive oxygen species. Finally, we answer the question whether the increased wound-healing is due to enhanced cell migration or proliferation.

Identifying the most relevant SAW parameters for cell stimulation

After the successful verification of the positive impact of SAW on cell growth in previous studies^{14,20}, we now elucidate adjustment parameters of the observed effect. In the first approach, we identified an increased cell growth of SaOs-2 cells up to 15.2 ± 1.7 % using Rayleigh-waves at $\lambda_{\text{SAW}} = 25 \mu\text{m}$ and $P_{\text{IN}} = 4 \text{ mW}$ ¹⁴. The high degree of variability of SAW-excitation raises the question which parameters might have the largest influence on cell stimulation. The physical properties of the SAW-depend on various parameters of the chip and the SAW-generating system. We here vary wave mode, wavelength, magnitude and shape or envelope of the SAW-amplitude. First, the employed piezoelectric substrate material and the direction of SAW-propagation with respect to the crystal axis defines the type and mode of the SAW. While Rayleigh-waves (RW) are excited on LiNbO_3 128° rot, Y-cut in the main direction, love-waves (LW) can be generated on LiTaO_3 40° rot, X-Y-cut²². In contrast to the RW, the excited LW exhibit no surface deformation in z-direction but are horizontally polarized waves. Second, the propagation direction, wavelength and width of the sound path of the excited SAW are defined by the geometry and layout of the IDT being processed on the substrate surface. Third, by varying the rf-signal amplitude as a function of time an amplitude modulated (AM) SAW of variable intensity can be generated.

Wave length

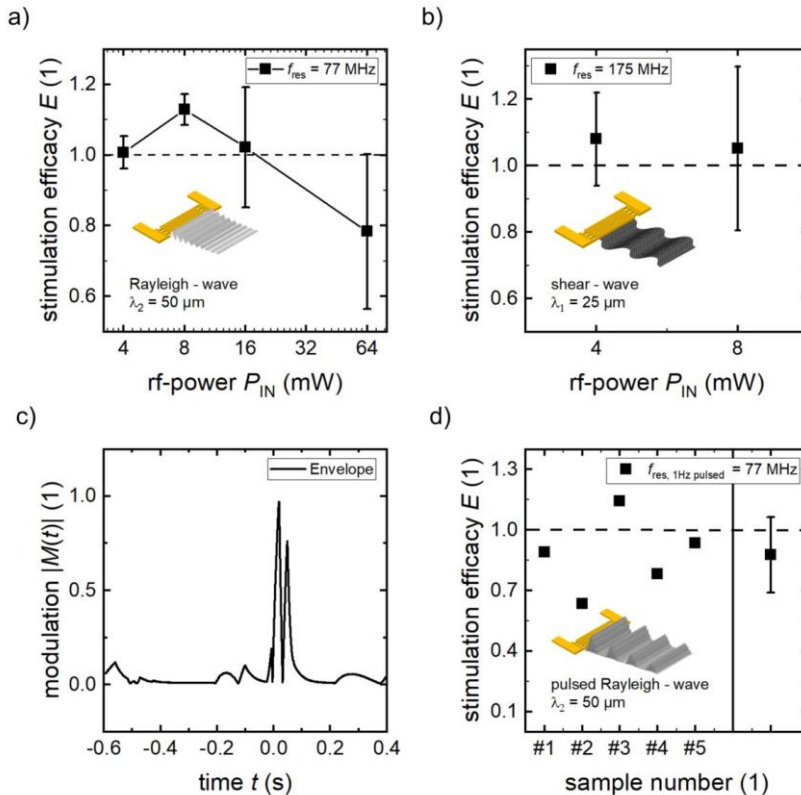


Figure 2: SAW-stimulated cell growth at varying physical properties of the excited SAW: a) Stimulation at different power levels at a wavelength of $\lambda_2 = 50 \mu\text{m}$ (mean and standard deviation of four independent measurements each), b) changing SAW-mode to shear-waves, c) amplitude modulated signal for the pulsed modulation shown in d). Median time for surface-coverage with SaOs-2 cells is about 60 hours.

In Fig. 2 the results of experiments with different SAW characteristics are shown. Changing the IDT periodicity from $\lambda_1 = 25 \mu\text{m}$ to $\lambda_2 = 50 \mu\text{m}$ leads to an accordingly reduced resonance frequency. In Fig. 2 a) we show the stimulation efficacy E in dependence of the applied power level P_{IN} . While there is no impact on cell growth at low power levels, the efficacy reaches its maximum $E = 1.13$ for $P_{\text{IN}} = 8 \text{ mW}$, indicating a slightly but significantly increased cell migration rate. With increasing SAW-

intensity, the cell migration is impeded, though. At a high power level of $P_{IN} = 64$ mW the rate is observed to decrease by as much as 20 %.

Wave mode

The results shown in Fig. 2 b), negatively answer the exciting question whether also shear waves with particle displacement in the plane of the surface of the substrate only increase cell growth. In contrast to the successful stimulation with Rayleigh waves at $P_{IN} = 4$ mW, there is only a slight and not significant increase of 8 % for LW mediated stimulation.

Pulsed excitation

As under physiological conditions also pulsatile pressure fields can appear, we exemplarily modulated the SAW-intensity by the absolute values of the cardiac function $M(t)$ shown in Fig. 2 c). The modulation frequency was set to $f = 1$ Hz imitating the resting pulse ($\lambda_2 = 50$ μ m). While the peak value is $P_{IN} = 16$ mW, the mean output is $\overline{P_{IN}} = 1$ mW. Using these settings, the power range between $0 \text{ mW} < P_{IN} < 16$ mW is covered, which leads to a positive effect for continuous SAW (CW) stimulation (Fig. 2 a)). However, as shown in Fig. 2 d), only one out of five experiments resulted in a slightly positive effect, while on average, the cell growth is reduced as compared to the reference. Thus, in contrast to CW stimulation, an AM or pulsed SAW in the same power range has no or even a slightly negative impact on cell growth.

These data demonstrate that positive SAW-mediated cell stimulation strongly depends on the physical properties of the SAW. A wavelength of the order of the cell diameter and a vertical surface displacement component of the SAW for a gentle power level in the magnitude of $O(10^0 \text{ mW})$ turned out to yield the strongest effects for SaOs-2 cells. The power dependency could be understood by the emerging negative effects accompanying SAW at high power levels: as shown earlier, there is a rise of substrate temperature of $\Delta T/\Delta P = 37 \text{ K/W}$ with increasing power (shown for $\lambda_1 = 25$ μ m)¹⁴. At a power level of $P_{IN} = 64$ mW a theoretical temperature rise of up to $\Delta T = 2.4 \text{ K}$ is expected, where we assume an equal temperature rise for λ_1 and λ_2 . However, this value exceeds the physiological temperature fluctuations and may harm the cells.

Conservation of SAW-enhanced cell growth for other cell lines and collective cell migration

The experiments presented above used culture of bone cancer cells SaOs-2. This mesodermal cell line has no polarity, a high motility and gap-junctions²⁸. Moreover, these cells, for their in vivo positions, do not necessarily require collective cell migration. In contrast, ectodermal cell lines have an apical and basal side forming a confluent cell layer with tight junctions. As one of their main purposes is to separate, to cover and to protect the underlying tissue, the process of regeneration and wound-healing is essential. Therefore, a supported wound-healing not only for bone fractures but also for epithelial cells, as for example the dermis, would be highly interesting. To investigate the effect of SAW-mediated stimulation on ectodermal cells, in the following experiments we used the model cell line MDCK-II.

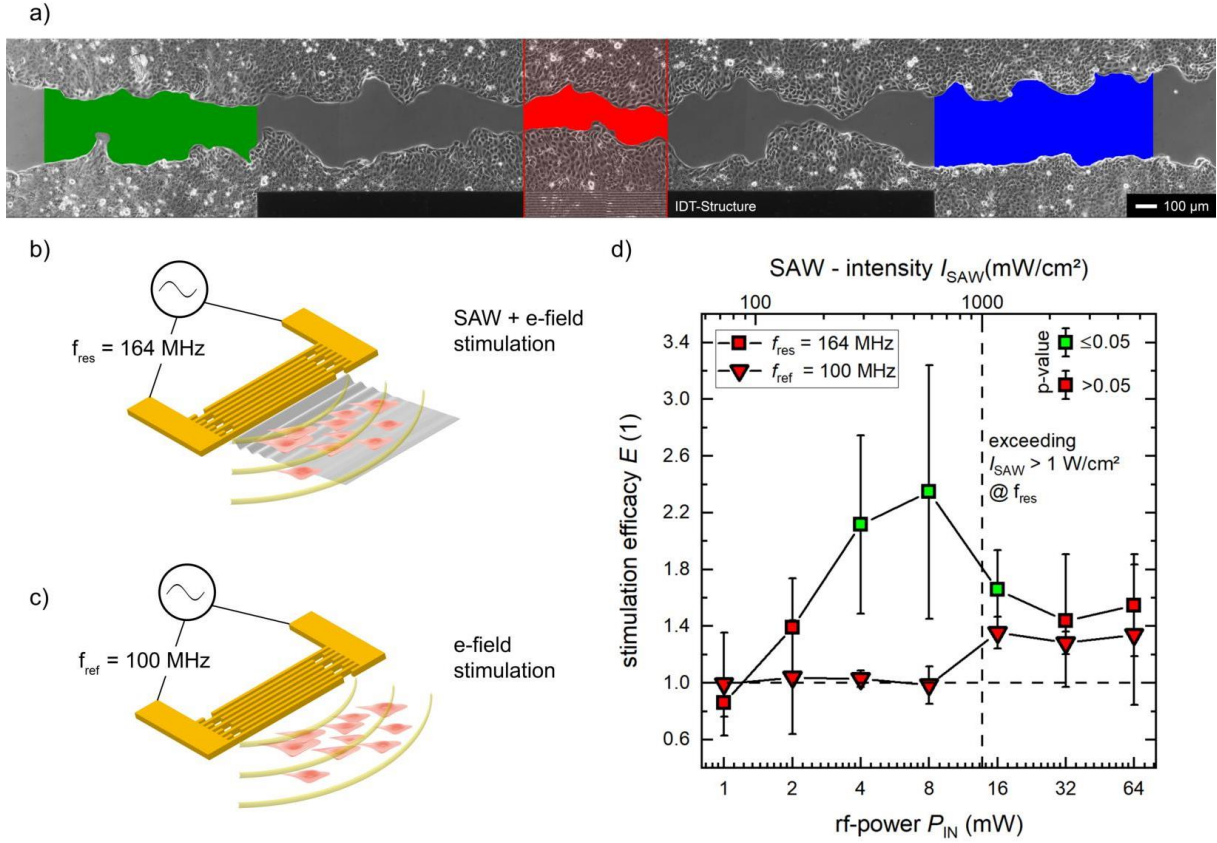


Figure 3: SAW-stimulation of the ectodermal cell line MDCK-II. a) High-quality micrograph image of the progressive *in vitro* wound-healing in a confluent monolayer at $t = 5$ h. The colored regions are indicating the SAW-stimulated cells (red) and the internal references (green, blue) b) c) representation of the different stimuli mechanism at different frequencies. While there is a simultaneous mechanical and electrical stimulation at the SAW-resonance frequency, we depict in b) the result of an electrical stimulus, only. This is achieved by detuning the IDT frequency to a somewhat lower value outside its bandwidth, where no SAW is excited (c). d) Power dependency on SAW-stimulation at different frequencies. Significant improvement of cell growth and migration rate up to $135 \pm 85\%$ for SAW-supported cell growth at $P_{IN} = 4$ mW and 8 mW. Exceeding $I_{SAW} > 1$ W/cm² leads to a decrease of E . A significant increase of the efficacy ($p < 0.05$) compared to an external low control is indicated by the color of the symbols inner area. The median time for surface-coverage with MDCK-II cells is about 31 hours.

Fig 3. a) shows the invading cell front of MDCK-II cells five hours after launching the SAW and thus the stimulus. In contrast to the SaOs-2 cell species, MDCK-II cells migrate collectively, eventually establishing a clear and sharp edge of the cell layers. Moreover, this single snapshot already indicates a bulge in the vicinity of the aperture due to increased cell migration velocity as a result of the SAW-stimulation.

Between the electrodes of an IDT and within the travelling piezoactive SAW, large electrical fields up to $O(1$ kV/cm) are created. According to the model of Datta²⁹, the surface potential Φ is related to the acoustic power P_{SAW} described by the equation

$$P_{SAW} = \frac{1}{2} \frac{W}{\lambda_{SAW}} y_0 |\Phi|^2.$$

Here, W is the width of the aperture and y_0 the material-dependent characteristic admittance $y_0 = 0.21$ mS for LiNbO₃ and the cut used in our experiments. This results in a surface potential ranging from $\Phi = 0.3$ V for $P_{IN} = 1$ mW up to $\Phi = 2.4$ V for $P_{IN} = 64$ mW. Thus, the IDT can also be regarded as acting as a dipole transmitter. Therefore, cells in the vicinity of the electrode and along the SAW's sound path are stimulated by an electrical field. As reported earlier, electrical rf-fields in the MHz

domain can actually act anti-inflammatorily and this way also promote the healing process³⁰. To separate the effect of electrical and mechanical stimulus, we performed reference measurements at a frequency $f_{\text{ref}} = 100$ MHz outside the bandwidth around the resonance frequency ($f_{\text{res}} = 164$ MHz). While the cells along the sound path at $f = f_{\text{res}}$ are stimulated mechanically and electrically in parallel (as illustrated in Fig. 3 b), cells in the reference measurement at $f = f_{\text{ref}}$ only experience the electric fields of comparable frequency and intensity (as illustrated in Fig. 3 c)).

In Fig. 3 d) the efficacy E at $f = f_{\text{res}}$ shows a pronounced increase in the power level range between $P_{\text{IN}} \in [4 \text{ mW}; 16 \text{ mW}]$ with a maximum at $P_{\text{IN}} = 8 \text{ mW}$. Cell growth in the SAW-stimulated area is up to 2.35 ± 0.73 times increased compared to the internal reference. The calculated p -values in this interval are $p_{4 \text{ mW}} = 0.02$; $p_{8 \text{ mW}} = 0.03$; $p_{16 \text{ mW}} = 0.03$ concluding a significant increase at a 5% level of significance. Further increasing of the SAW-intensity I_{SAW} above 1 W/cm^2 results in a decrease of the efficacy E . This is in accordance with the observed decreased healing rate in US-treatment mentioned above¹². However, no significant increase of the efficacy E can be determined for values $P_{\text{IN}} \geq 32 \text{ mW}$. At power levels of $P_{\text{IN}} = 128 \text{ mW}$ and above, cells are either detached from the substrate surface or becoming necrotic within minutes to hours. Taken together, not in a single experiment, A_{mig} of the internal reference sections was higher than A_{mig} in the sound path for values $P_{\text{IN}} \geq 2 \text{ mW}$.

In contrast, there is no evidence for a positive stimulus at $f_{\text{ref}} = 100$ MHz where no SAW is excited but a comparable electrical field is present. Here, the 5% level of significance is never reached for a single power level. For $P_{\text{IN}} = 16 \text{ mW}$ and higher, a slight effect in the reference measurements is observed. This could be understood by the generation of finite amplitude SAW even outside the bandwidth of the IDT for high power levels. In Fig. 4 a) we depict the typical return loss S_{11} of an IDT as a function of frequency. While for this chip the return loss at the resonance frequency is $S_{11} = -18.59 \text{ dB}$, it is much weaker at the reference frequency with $S_{11} = -0.93 \text{ dB}$. Thus, the intensity of the SAW for both frequencies f_{res} and f_{ref} differs by about 18 dB! Thus, at low power values, the SAW-generation can safely be neglected at the reference frequency f_{ref} . However, increasing the applied power level eventually leads to an appreciable SAW-generation but still much weaker as compared to the one at the resonance frequency f_{res} for the same applied power P_{IN} .

These findings are supported by the exemplarily shown superimposed images in Fig. 1 d-1) – d-3). Here, the *in vitro* wound-healing process for a SAW (d-1)) and electrical field (d-2)) treated as well as an untreated sample (d-3)) is displayed. By comparing the three given images, the most pronounced cell migration is visible in the SAW-stimulated sample. Whereas the internal references are exhibiting reddish colors, the hues in front of the aperture appear to be violet and blue shaded. In contrast, in the next two images, only an electrical field was applied and an external reference with no stimulation indicates a uniform growth rate along the complete gap.

In analogy to previously published experiments (Stamp, Brugger et al. 2016)¹⁴ we applied Rayleigh waves with a wavelength of $25 \mu\text{m}$ at power levels of $P_{\text{IN}} = 2 \text{ mW}$ and 4 mW to SaOs-2 cells. But, we additionally added a 10 nm thick conductive titanium layer on top of the sound path, as indicated in the SI-Fig. 3. Compared to the same experiments but without shielding layer no significant difference in increase of cell growth was found ($15 \pm 2\%$ vs. $12 \pm 5\%$). In these experiments the mechanical stimulation nearly remains unchanged but lateral electrical fields are shortened completely and vertical electrical fields are shielded to some extent. These data further support our conclusions excluding electrical fields as major contribution to the observed effect.

Further indications that the electrical fields are no major contributor to the effect, are the results shown in Fig. 2 b). Shear waves are accompanied by electrical fields of the same order of magnitude but do not lead to significant increased *in vitro* wound healing.

Moreover, we performed additional reference measurements regarding the agitation of medium. Here, the IDT ($\lambda_{\text{SAW}} = 25 \mu\text{m}$) is placed aside the gap inducing streaming by Leaky-SAW at a power level of $P_{\text{IN}} = 4 \text{ mW}$. Therefore, the cell culture is only affected by the streaming. A comparison to external references without SAW application running in parallel demonstrates no significant impact on the cell growth ($E = 0.97 \pm 0.33$). For further details, see the SI.

However, to allow for quantitatively comparing the SAW induced streaming with literature and to understand the cell-stimulating mechanical forces, the well-known acoustic streaming effect³¹ that is proportional to the SAW-intensity, is measured quantitatively. Fig. 4 b) shows the flow-profile evaluated at a height $h = + 25 \mu\text{m}$ above the substrate measured by sPIV. The liquid is drawn towards the IDT and then streams upwards under the Rayleigh angle. Mean velocities are measured for both, the SAW illuminated region and the internal reference. Both regions are compared in Fig. 4 c), while the mean flow speed near the center of the artificial wound in front of the aperture is labeled with *) and parallel in the internal reference with **). As expected for $f=f_{\text{res}}$ the velocity increases linear with the applied power level until it reaches its measured maximum of $v_{\text{as}} = 1.2 \text{ mm/s}$ at $P_{\text{IN}} = 128 \text{ mW}$. For $f=f_{\text{ref}}$ only slight streaming appears for $P_{\text{IN}} \geq 32 \text{ mW}$. For $P_{\text{IN}} = 128 \text{ mW}$ the streaming velocity is comparable to the one at f_{res} at $P_{\text{IN}} = 1 \text{ mW}$ at the magnitude of $O(10^{-2} \text{ mm/s})$.

The maximum velocity of $v_{\text{as}} = 1.2 \text{ mm/s}$ results in a dynamic pressure q

$$q = \frac{\rho}{2} v^2 = 6.05 \cdot 10^{-4} \text{ Pa}$$

and a shear stress τ

$$\tau = \eta \frac{\Delta v_{\text{as}}}{\Delta z} = 0.47 \text{ dyne/cm}^2.$$

Here, ρ reflects the density of water and $\eta = 0.97 \text{ cP}$ the viscosity of medium with 10 % FBS at $T = 37 \text{ }^\circ\text{C}$ ³². If the observed effect was only a simple result due to streaming, the flow field generated here would result in an asymmetric artefact in the observed cell migration: cells on the IDT-side, denoted as the 'downstream' side, have to migrate against the direction of flow while the opposing cells migrate along the flow denoted as 'upstream'. This would result in a non-uniform, even asymmetric wound closure. To identify such possible differences in the migration speed as illustrated in Fig. 4 e), the velocities of both opposing cell fronts (luv and lee) are shown in Fig. 4 d). All data points scatter around the bisector with a very slight tendency to the upper side.

The ratio $v_{\text{IDT-side}}/v_{\text{IDT-opp}}$ is smaller than 1 for 65 % of the data points for f_{res} and 59% for f_{ref} , respectively. The average values are $v_{\text{IDT-side}}/v_{\text{IDT-opp}} = 1.08 \pm 0.67$ and $v_{\text{IDT-side}}/v_{\text{IDT-opp}} = 0.95 \pm 0.61$ for SAW and electrical field stimulation, respectively. This indicates that the streaming effect on cell migration is indeed weak and thus can be neglected in our data analysis. If the cells migrate faster, this holds for both sides of the gap.

These data demonstrate the positive effect of SAW-stimulation on cell growth. In a narrow SAW-power interval, a significant increase of the surface-coverage rate can be observed, where lower intensities have no significant impact and very high intensities are observed to impede the cell growth. Furthermore, the comparison between the SAW-stimulated area and the internal reference strongly support the assumption that only the mechanical component of the piezo active SAW is the main reason for the effect and is not outweighed by spurious, accompanying side effects like temperature, fluid flow or electrical fields.

Possible reasons for our findings could be an enhanced proliferation or an increased cell activity as well as an increased cell migration for cells residing in the sound path. To narrow down the underlying mechanisms and to characterize potentially negative impacts of the SAW-stimulation on cells at very high SAW-intensities, the proliferation of cells and the production of intracellular ROS was analyzed.

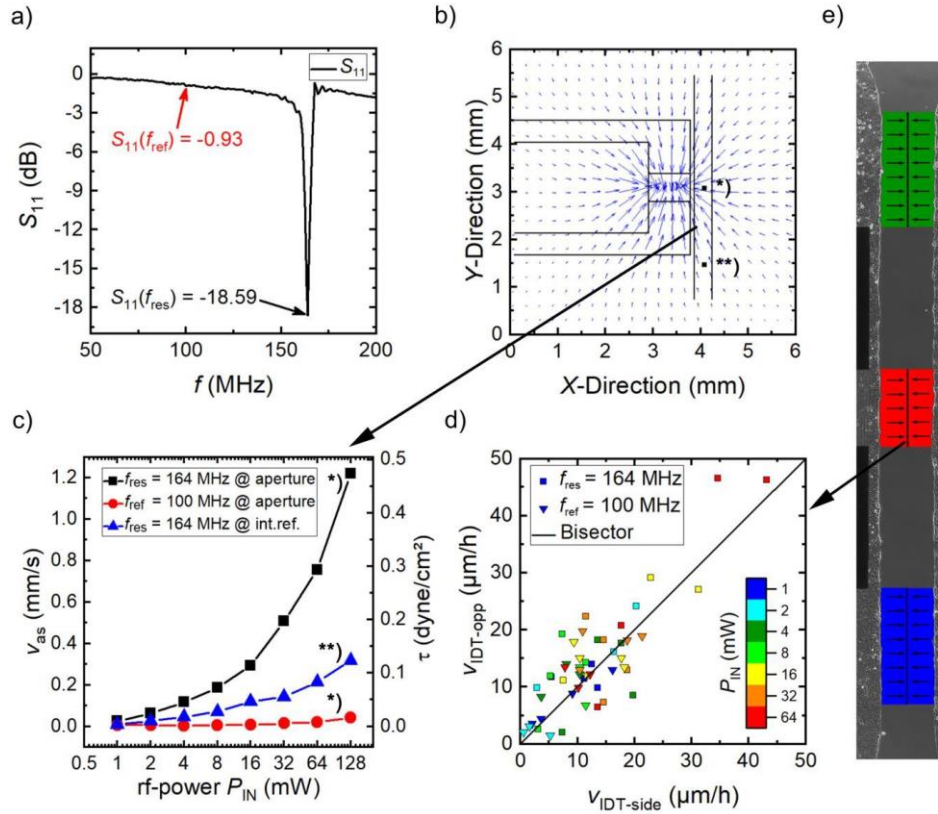


Figure 4: Physical properties of the experimental setup and the cellular response. a) The return loss S_{11} is strongly frequency-dependent. While for $f=f_{res}$, a SAW is resonantly excited, at $f=f_{ref}$ only the electric field stimulates the cells. b) To estimate the SAW-intensity at different power levels P_{IN} and to characterize the flow profile, a SIV measurement was performed at a height of $h=+25$ μ m above the substrate. The liquid is streaming towards the aperture. The streaming velocity v_{as} was determined at the aperture *) and the internal reference **) c) power- and location-dependent streaming velocity $v=v_{as}$ d) The small asymmetry of the flow profile has no significant impact on the migration velocities of the opposing cell fronts in e).

The influence of SAW-stimulation on intracellular mechanisms

In order to understand the significant increase of the stimulation efficiency for MDCK-II cells at $P_{IN} = 4 - 8$ mW, cellular parameters, like cellular stress and proliferation are measured by fluorescence imaging. ROS are indicators of cellular stress and play a significant role in programmed cell death or necrosis by activating signal cascades and inducing or suppressing gene expression³³. Therefore, they are a valuable indicator to determine negative side-effects of SAW-stimulation. In contrast, proliferation in healthy cells, is an actively controlled mechanism and is regulated by multiple signals ranging from growth factor signaling to DNA damage, developmental cues³⁴, mechanical manipulation³⁵ and spatial restrictions^{36,37}. In these experiments, we extended the power range and also included a very high power level of $P_{IN} = 128$ mW to explore the limits of SAW-stimulation.

Stress level - ROS

In our experimental setup, both mechanical forces and possible thermal effects induced by the high SAW-intensities act on the whole cell culture. To qualify any potential negative effects, the concentration of ROS in the cells residing within the SAW-inflicted area is compared to the internal reference as well as an external 'low' and 'high' control. In the SI a typical image of the intracellular

stress of SAW-stimulated cells at a power level of $P_{IN} = 64$ mW is shown. The quality of the cell layer and possible morphological changes are verified for each sample using phase contrast imaging. No morphological changes were identified for values $P_{IN} \leq 64$ mW. The position information of the nuclei in selected regions are used to determine the cellular stress level as a function of the applied power level P_{IN} as displayed in SI-Fig. 5. For the complete power range tested, the experimental conditions of the cells close to the aperture remains the same as for the internal reference or low control. Therefore, there is no significant increase of ROS due to SAW-stimulation for the tested power range between $P_{IN} = 8$ mW to 64 mW. At very high SAW-powers ($P_{IN} = 128$ mW), some cells start to become ripped off the substrate *inter alia* caused by the high shear stress induced by the acoustic streaming. Furthermore, the cell coverage rate is significantly decreased for the complete culture as it can be seen by the gap still being present after 24 hours. At high intensities, the temperature in the culture media increase due to a SAW-related substrate heating. At a power level of $P_{IN} = 128$ mW, the above mentioned substrate heating, for example, results in an increase of the bulk media temperature from about $T_{P=0 \text{ mW}} = 36.6$ °C to $T_{P=128 \text{ mW}} = 39.1$ °C, thus exceeding the ideal culture conditions. Therefore, the data points for $P_{IN} = 128$ mW are poorly suited for this measurement and this power value marks a threshold: For higher intensities like, e.g., $P_{IN} = 256$ mW cells become necrotic and are removed from the substrate in the area around the aperture.

This concludes, that there is no SAW-induced increase of intracellular ROS for a reasonable range of power levels ($P_{IN} \leq 64$ mW). The cellular stress level remains in the normal range as proven by the identical condition of treated and untreated cells for ideal SAW-parameters, as shown before.

Proliferation

The proliferation of cells is regulated and stimulated by mechanical forces, electrical stimulation, spatial restrictions and others mechanisms^{35,37,38}. We demonstrate a positive impact of SAW on the proliferation rate in the SAW-irradiated samples. Since not only cells in the sound path but also in the internal reference are stimulated, enhanced proliferation can be excluded as the main reason for the increased efficacy E shown above.

For a conclusive evaluation, the proliferation rate was determined along the SAW sound path at the artificial wound and inside the confluent cell layer and compared to the corresponding internal and external reference. In Fig. 5 a), proliferated cells of a large area around the IDT structure are displayed. In the upper section of the image, the tapering of the cell layer marks the section of the former gap, while the lower section shows the domain of the initial cell layer. Selected regions indicated by the colored rectangles ($\Delta x = 300$ μm , $\Delta y = 650$ μm) are evaluated in accordance with the ROS measurements. Red marks the *front aperture* area and blue the *rear* of the aperture. Yellow and green, respectively, indicate the corresponding *internal references*. Fig. 5 b) – d) display a section of the cell layer in front of the aperture. The phase contrast image in Fig. 5 b) is used to verify the cell layer's quality, while Fig. 5 c) shows the nuclei of all cells and Fig. 5 d) only the cellular nuclei with freshly synthesized DNA. The labeled areas are evaluated statistically as described previously. Each measurable is depicted as a small inset above the corresponding graphs. All data points for one power level represent samples from the same cell passage prepared at the same day. In the external references, no SAW was employed at all, although the rest of the setup was prepared analogously to the other samples. Fig. 5 g)-h) show the absolute proliferation rate depending on the applied power level P_{IN} in the front and rear of the aperture. The gray shaded areas correspond to the standard deviation of all external references. Fig. 5 i) shows the relations between the front and rear region of the IDT in the sample and in the external reference. Fig. 5 j)-k) displays a comparison on the relative proliferation rate $X(P_{IN})$ between the samples and the external references. For the consideration of the actual cell density, Fig. 5 l) characterizes the post-mitotic mean area per cell A in the external references independent from eventual SAW-induced stimulation effects.

In Fig. 5 g) and h), the course of the absolute proliferation X_{abs} in the stimulated area in the sound path is nearly identical to the internal reference for a wide range of the applied power levels P_{IN} for both the front and the rear side of the IDT. In Fig. 5 g), distinct maxima for $X_{\text{abs-aperture}}(8 \text{ mW}) = 0.88 \pm 0.05$, and $X_{\text{int. ref.}}(8 \text{ mW}) = 0.86 \pm 0.05$, respectively are observed as compared to the external reference $X_{\text{ext. ref.}}(8 \text{ mW}) = 0.68 \pm 0.12$. Furthermore, at a very high power level $P_{\text{IN}} = 128 \text{ mW}$ a significant decrease in the front aperture becomes visible $X_{\text{abs-aperture}}(128 \text{ mW}) = 0.43 \pm 0.11$.

Thus, we state that there is no significant difference in the proliferation rate of cells in the sound path to cells in the internal reference. However, an increase of $X(P_{\text{IN}})$ is ascertainable when considering the proliferation of the treated samples relative to the external reference. $X(P_{\text{IN}})$ is increased for a wide range between $P_{\text{IN}} = 4 \text{ mW} - 64 \text{ mW}$ as shown in Fig. 5 j). The maximum values are reached at $P_{\text{IN}} = 4$ and 8 mW with p -values of $p_{4 \text{ mW}} = 0.058$ and $p_{8 \text{ mW}} = 0.049$ which corresponds to the maximum for the surface-coverage rate of Fig. 3 d). At $P_{\text{IN}} = 128 \text{ mW}$ the relative proliferation rate decreases only at the aperture to $X(128 \text{ mW})_{\text{rel-SAW}} = 0.68$ ($p_{128 \text{ mW}} = 0.033$) in contrast to the internal reference $X(128 \text{ mW})_{\text{rel-int. ref.}} = 0.98$. For cells inside the layer (Fig. 5 k)), this effect is not very pronounced but still a significant increase of X_{rel} is measurable for $P_{\text{IN}} = 4 \text{ mW}$ with $X_{\text{rel-SAW}}(4 \text{ mW}) = 1.55 \pm 0.51$ ($p_{4 \text{ mW}} = 0.027$) and a decrease for $P_{\text{IN}} = 128 \text{ mW}$ with $X_{\text{rel-SAW}}(128 \text{ mW}) = 0.053 \pm 0.226$ ($p_{4 \text{ mW}} = 0.034$).

The comparison of the absolute values in the sound path at the front with the proliferation rate inside the layer obviously exhibit fluctuations (Fig. 5 h)). Cells in the front always proliferate more than in the back. Here, SAW-dependent effects can be excluded as the external reference shows the same course (Fig. 5 i)). This might be a consequence of the actual state and density of the cell culture for the day of the experiment. Cells at the edges, moreover, can cover a larger surface than cells inside the layer (Fig. 5 l)).

If we compare the mitosis of the cells at the edges of the layer having a low areal density to those cells being tightly packed in the layer, we observe a continuously higher proliferation rate (Fig. 5 i)) for the first. This matches the fact that the division rate is known to slow down with decreasing cell-free space. Puliafito et al.³⁷ reported on a critical cell area of about $A_{\text{crit}} = 200 \mu\text{m}^2$, below which the cell division rate dramatically decreases. They argue that this decrease is due to cell contact inhibition. As cells at the edges of the cell layer can acquire more space, they proliferate more than cells inside of the layer. As shown exemplarily in Fig. 5 e) and f), the available space per cell in the gap area after 27 h with a median of $A = 193 \mu\text{m}^2$ is still larger than the one in the interior of the layer with $A = 170 \mu\text{m}^2$. In Fig. 5 f), we depict the appearance of cell domes (marked in blue) because of the high cell density. The phenomenon of contact inhibition³⁷ can also explain the distinctive drop in the relative proliferation rate at $P_{\text{IN}} = 16 \text{ mW}$ and 32 mW in Fig. 5 j). In these distinct experiments, a spatially confined impairment of the cell proliferation occurred due to an accidentally too high cell density in the critical cell area range. Note, that the proliferation rate in the rear section of the sound path is significantly increased to $X(4 \text{ mW}) = 1.55 \pm 0.51$ ($p_{4 \text{ mW}} = 0.027$) even though the cell density fluctuates around A_{crit} in the sample as well as in the internal reference.

Our data are clearly consistent with a significant effect of SAW-stimulation on the proliferation of cells. Cells being actively irradiated by SAW proliferate up to $29 \pm 23 \%$ more than in the external reference. The fact that cells in the internal reference proliferate similarly to the ones in the sound path is attributed to streaming effects. As there is a measurable flow in the whole culture as shown in Fig. 4 c), the cell media is actively stirred²³ reducing the local metabolite concentration and increasing the gas exchange as compared to a diffusion-limited static culture³⁹. The obvious decrease for high power levels at $P_{\text{IN}} = 128 \text{ mW}$ may result from high shear forces simply detaching the cells from the substrate. While cells in the interphase are firmly attached to the culture surface, cells round up in the M phase and are therefore are much more loosely attached to the surface⁴⁰. The acting shear stress of about $\tau \approx 0.47 \text{ dyne/cm}^2$ for the measured streaming velocity of $v = 1.2 \text{ mm/s}$ at $P_{\text{IN}} = 128 \text{ mW}$ is apparently

high enough to remove mitotic cells in the vicinity of the aperture. This subsequently results in a decreased proliferation rate. Furthermore, as explained in the ROS measurements, any SAW-induced temperature increase of the media could harm the cells.

Greco et al.²⁰ recently demonstrated positive and negative effects on cell proliferation upon SAW-stimulation, also depending on two distinct applied power levels. Our data, however, presume a two-stage threshold effect for a wide power range. Remaining largely unmodified for low SAW-intensities, the proliferation rate $X(P_{IN})$ increases if the SAW-induced media stirring is strong enough. The rate is independent from the actual streaming velocity and SAW-power level P_{IN} , as long as the diffusion limitation for media supply is overcome. After reaching a second threshold, the effect reverses and the proliferation is decreased.

The fact that the proliferation in the whole culture is positively affected by the SAW treatment suggests that proliferation alone cannot be the cause for the increased surface-coverage of cells in the sound path compared to the internal reference.

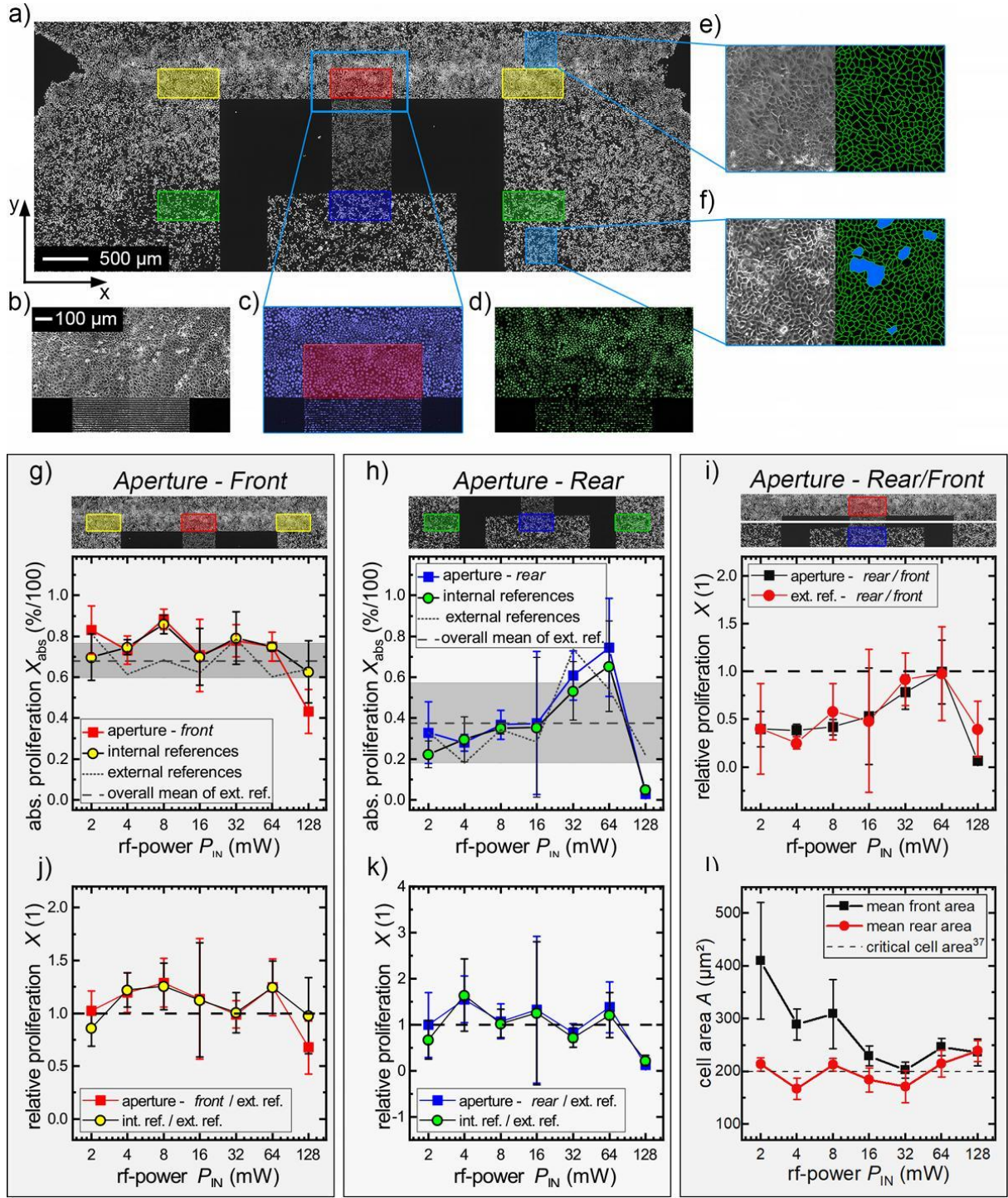


Figure 5: Determination of the SAW-induced influence on cell proliferation. a) Fluorescence image of nuclei with newly synthesized DNA with evaluated regions marked in different colors (red: front aperture, yellow: internal reference front, blue: rear aperture, green: internal reference back). b) – d): Images of the artificial wound in phase contrast (b)), all cellular nuclei (c)) and newly synthesized (d)). e)/f) Phase contrast images and cell border of the cell layer. e) MDCK-II at low density (wound) f) MDCK-II at high density with emerging cell domes (blue spots). g)/h) Absolute proliferation $X_{\text{abs}}(P_{\text{IN}})$ of the front and rear area. i) Relative proliferation inside the cell layer and at the edge. j)/k) SAW-stimulated samples compared to external references. l) Average area per cell in the corresponding external reference in the front and rear section of the aperture. Cultivation time for measurement point at $P_{\text{IN}} = 16$ mW $t = 22$ h, else $t = 27$ h.

Discussion

The results of this study clearly indicate the high impact of SAW-mediated cell stimulation on the closure of an artificial wound in a cell monolayer in a distinct power range. The surface-coverage rate in the sound path is increased up to 135 %, compared to an internal reference and depending on the experimental conditions. For the increased surface-coverage rate, a variety of different mechanisms like increased proliferation, cell activation or enhanced cell spreading and migration may be considered. In earlier wound-closure studies^{41,42}, cell spreading and migration rather than enhanced proliferation had already been assigned to be the major mechanisms for in vitro wound-closure.

In the following we exclude enhanced proliferation or acting shear forces as the main reasons at low power levels for the increase in stimulation efficacy. Then, we narrow down the remaining cause of the observed effect to increased cell migration evoked by the mechanical, not electrical component of the SAW. Moreover, we discuss that this mechanical stimulation can influence the intracellular calcium concentration and therefore the migration rate. Finally, we argue that a mechanic stimulation can explain also negative effects for a pulse modulation.

As we find an increased cell proliferation on the whole chip rather than only in the sound path, a higher mitotic rate can be ruled out for our findings of increased wound-healing in the sound path. Therefore, only cell migration and spreading may be the reason for increased surface-coverage. Reasons for an enhanced migration vary widely and can be influenced by signaling molecules, cell activation state or external forces. For instance, it has been suggested that wounding, as given in our case, causes the release of signaling molecules or growth factors to promote cell motility⁴³. Laminar flow towards the IDT should promote the convective transport of chemokines to cells on the IDT side to enhance the migration. Since both sides migrate in the same manner, it is unlikely that enhanced cell migration was due to an enhanced transport of signaling molecules.

Another point to consider is cell stimulation evoked by shear flow. As shear forces are important modulators of endothelial cells, they influence important functions like cell elongation, formation of stress fibres, increased permeability, secreting chemoattractants, activation of G-proteins and so forth^{44,45}. However, the cellular alteration depends on the shear magnitudes: distinct changes in cell morphology and orientation ($>8 \text{ dyne/cm}^2$)^{46,47}, chemoattractant secreting ($>9.8 \text{ dyne/cm}^2$)⁴⁸, influenced migration direction ($>3 \text{ dyne/cm}^2$)⁴⁹, activation of protein kinases ($>0.5 \text{ dyne/cm}^2$)⁵⁰ or inhibition of apoptosis ($>15 \text{ dyne/cm}^2$)⁵¹. Furthermore, it has been shown that low shear rates ($< 4 \text{ dyne/cm}^2$) can enhance proliferation and differentiation for osteoblasts and fibroblasts^{52–54}. Concerning the cell migration, Hsu et al. demonstrated for high shear stresses (17 dyne/cm^2) an increased migration rate at wound edges for laminar and disturbed flow conditions compared to static cultures⁵⁵. Especially laminar flow facilitates cell migration by promoting of cell-cell junction disruption and focal adhesion dynamics or mechanical pushing effects. Furthermore, intracellular signaling pathways like small GTPase Rho and tyrosine kinases are stimulated under high shear conditions promoting cell motility⁵⁵.

In the power range of $P_{\text{IN}} = 4 - 8 \text{ mW}$ the maximal shear stress is 0.07 dyne/cm^2 and consequently based on literature cited above too small to remarkably stimulate cells. If the effect simply was a consequence of shear stress, the absolute values of the surface-coverage rate for the internal references would have to increase with increasing power. This is not the case. Induced activation through shear forces are therefore also out of the question.

However, for higher values above $P_{\text{IN}} \geq 32 \text{ mW}$ the effective shear force exceeding 0.2 dyne/cm^2 might no longer be negligible. Cells may be stimulated inducing *e.g.* the activation of protein kinases. But at the same time negatively affects due to a temperature increase might appear.

A local substrate heating results in a linear increase of the substrate temperature $\Delta T_s = 37 \frac{\text{mK}}{\text{mW}} P_{IN}$ for power levels below 100 mW. Therefore, at values $P_{IN} \geq 32$ mW the physiological fluctuations of $\sim \pm 1$ K are exceeded what might harm the cells.

Thus, at high power values cells in the sound path are simultaneously affected by positive and negative influences ($I_{SAW} > 1 \text{ W/cm}^2$, $T_s > 38^\circ\text{C}$). The cells in the internal reference may also be positively affected by the increased shear force ($\tau > 0.1 \text{ dyne/cm}^2$ for $P_{IN} = 128$ mW). This might result in an overall decreased relative efficacy E for high power values.

Consequently, we exclude enhanced proliferation or acting shear forces as the main reasons at low power levels for the increase in stimulation efficacy. Up to this point increased cell migration evoked by mechanical or electrical stimulation remain as the only possible and plausible causes. As there is no evidence for cell stimulation at f_{ref} (Fig. 3 d)) the electric component of the SAW can also be excluded.

This leads to the question, how cells could react on such a mechanical stimulation. Through the mechanical component of a SAW cells along the sound path undergo mechanical vibrating, pressure and deformation forces. By the fact that most cells are mechanosensitive^{56,57}, a cellular response on these acting forces can be expected. A possible response would be a change in the intracellular calcium concentration $[\text{Ca}^{2+}]_i$. In previous studies, it has been demonstrated that $[\text{Ca}^{2+}]_i$ can be increased by mechanically stimulating the cell membrane with a microprobe by discrete membrane deformation or stretching of the cell membrane⁵⁸⁻⁶⁰. If cells grow in a confluent monolayer, adjacent non-stimulated cells also show an increase of $[\text{Ca}^{2+}]_i$ up to a radius of 4 - 6 cells or a distance of up to $100 \mu\text{m}$ ⁵⁸. As calcium $[\text{Ca}^{2+}]_i$ is well known to play a crucial role in regulating cell migration (articles^{61,62}, reviews⁶³⁻⁶⁵), the mechanically induced calcium release could be a possible reason for the enhanced cell motility. The transmission of the Ca^{2+} -response across a confluent monolayer may explain the increased motility of non-stimulated cells in the vicinity of the sound path. In contrast, cells at the internal reference are too far apart to become influenced by SAW. The ineffectiveness of LW-waves can be traced back to the missing z-deflection of the substrate as LW are polarized horizontally and therefore missing substrate vibration. Summing up, a change of the intracellular calcium concentration can explain our observation.

Last but not least, a mechanical stimulation mechanism can help to understand the observed decreased efficacy for pulsed stimulation. Cells can adapt to mechanical stress by reorganizing the cytoskeletal structure or cell shape⁶⁶. Among other things, the cytoskeletal stiffness is increased in direct proportion to the applied stress⁶⁷. Dependent on the applied force shape and thus time constant, the cellular adaptation ranges from an immediate viscoelastic response, adaptive behavior with oscillatory forces, adaptive cell stiffening of adhesion structures with sustained static stress (>15 seconds) to large-scale repositioning response with prolonged (>1 minute) stress⁶⁸. This may explain the adverse effect of pulsed SAW on cell growth. Applying a constant force results in improved cellular adaptation compared to short 1 Hz pulses.

For future studies answering the so far open questions from a biochemical point of view, it is crucial to find a human cell line with a high transfection efficiency. We thus treated T-REX™-293 in identical experiments as described above ($P_{IN} = 8$ mW, $\lambda_{SAW} = 25 \mu\text{m}$). We here obtained a stimulation efficiency of $E = 1.24 \pm 0.08$ ($n = 4$, $p = 0.0003$). This further supports the claim that the observed effect is not limited to one or two single cell lines and opens up a whole range of possibilities to modify the studied cell line, to further narrow down the stimulation mechanism.

In total, the stimulation mechanism is a combination of substrate movement and shear stress. Depending on the applied power level P_{IN} the respective contribution on cell stimulation may differ. While at low power levels cells are positively affected only by mechanical vibration, the contribution

of shear forces and temperature can no longer be neglected for higher values and the positive effect turns around if the applied power level is too high. How the mechanotransduction of this stimulation in the MHz regime actually takes place in detail has to be further illuminated. It might contain even a 'rectifying' DC effect (cf acoustic streaming), acting via the pressure dependent density on the cell membrane and thus also the interior of the cell. Such a potential DC effect indeed would be consistent with the ineffectiveness of LW-Waves, as they do not excite waves into the medium. As we are still unable to really prove such hypotheses, we do not claim a specific mechanism here.

Conclusion and outlook

We here presented an in depth study of SAW-mediated cell growth for tissue stimulation and wound-closure. We employed SAW with different parameters on different cell lines and successfully identified their relevance in terms of enhanced cell growth. Rayleigh waves with a wavelength of the order of the size of the adherent cells are found to be most efficient in their influence on the cell growth. While employing a wide power range of the SAW, we identify a global maximum of the stimulation efficacy. For SaOs-2 cells, for example, this maximum turns out to be $E = 1.18$ for $P_{IN} = 8$ mW. For MDCK-II cells, for comparison, we find an even larger increase of up to 135 % (compared to the internal reference) in the power interval of $P_{IN} \in [4 \text{ mW}, 16 \text{ mW}]$.

As SAW on a piezoelectric substrate contain both, the mechanical as well as electrical components, we measure the surface-coverage rate at the SAW resonance frequency and a slightly different excitation frequency, where no SAW is generated but the electric fields around the transducer is basically the same. The fact, that SAW cells in the sound path at f_{res} migrate faster as compared to the 'no SAW' frequency f_{ref} confirms our hypothesis that the mechanical component is decisive for an enhanced surface-coverage.

Besides the main effect shown here, this technology also enables additional studies focusing on the extremely low shear force regime within one cell ensemble. A correlation of flow field and various cell responses could be performed in a similar manner as presented earlier for example of cell adhesion⁶⁹.

To understand the intracellular mechanisms which leads to an increased migration rate, the concentration of ROS and the proliferation of cells were measured. While the cellular stress remains equal to the low controls for the measured power spectra, a significant change in the proliferation for the whole stimulated sample was noticed. We demonstrated a two-step threshold for the proliferation. Remaining unmodified for low SAW-intensities, the proliferation increases for values above $P_{IN} \geq 4$ mW up to 29 ± 23 % compared to the external reference. Reaching a second point, $P_{IN} \geq 128$ mW, excessive SAW-intensities subsequently lead to a decrease in the measured proliferation. The reasons for the increased *in vitro* wound-healing are therefore not an increased proliferation rate of cells in the sound path, as all cells on the chip proliferate faster.

The exclusion of proliferation, ROS, temperature, shear force and electrical fields identifies the mechanical stimulation by vibration as the main cause for our observed phenomena of further enhanced *in vitro* wound-healing additional to overall increased proliferation.

Since cells can adapt to mechanical stress by reorganizing the cytoskeletal structure or cell shape⁶⁶, further studies should investigate the impact of known factors that regulate cytoskeletal structure or cell shape. Recently, for instance, an intramembrane protease was implicated in the regulation of proteoglycosylation^{70,71}, which strongly impacts on the composition of the extracellular matrix and, thus, cytoskeletal structure and cell shape. Furthermore, it would be highly interesting to determine the calcium response, cell activation or biomarker expressions. As cells, especially stem cells, are

influenced by the stiffness of the substrate⁷², an application of SAW-stimulation to influence differentiation would be very illuminating!

Transferring this fundamental result to a medical application of course is a completely new and additional task. A rough idea how this could be managed are arrays of transducers on flexible disposable substrates⁷³ that are inductively power supplied⁷⁴. Going even one step further could be transducers on implants that are supplied in the same way.

Acknowledgements

The authors thank the Cluster of Excellence 'Nanosystems Initiative Munich (NIM)' for funding. Special thanks to Sidonie Lieber, Alexander Hupfer and Andreas Hörner for technical assistance and Emeline Nysten for SEM of SAW. M.S.B. thanks the 'Stiftung der deutschen Wirtschaft (sdw)' for personal funding.

1. Buchegger, S. *et al.* Antibacterial metal ion release from diamond-like carbon modified surfaces for novel multifunctional implant materials. *J. Mater. Res.* **31**, 2571–2577 (2016).
2. Stejskalová, A., Oliva, N., England, F. J. & Almquist, B. D. Biologically Inspired, Cell-Selective Release of Aptamer-Trapped Growth Factors by Traction Forces. *Adv. Mater.* **31**, 1806380 (2019).
3. Knoch, H. G. Beitrag zur Wirkungsweise der Ultraschallenergie. *Schriften der Med. Akad. Dresden* **6**, 81–87 (1967).
4. Klug, W., Franke, W.-G. & Knoch, H.-G. Scintigraphic control of bone-fracture healing under ultrasonic stimulation: An animal experimental study. *Eur. J. Nucl. Med.* **11**, 494–7 (1986).
5. Kristiansen, T. K., Ryaby, J. P., McCabe, J., Frey, J. J. & Roe, L. R. Accelerated Healing of Distal Radial Fractures with the Use of Specific, Low-Intensity Ultrasound. A Multicenter, Prospective, Randomized, Double-Blind, Placebo-Controlled Study*. *J. Bone Jt. Surg.* **79**, 961–73 (1997).
6. Binder, A., Hodge, G., Greenwood, A. M., Hazleman, B. L. & Page Thomas, D. P. Is therapeutic ultrasound effective in treating soft tissue lesions? *Br. Med. J.* **290**, 512–514 (1985).
7. Heckman, J. D., Ryaby, J. P., McCabe, J., Frey, J. J. & Kilcoyne, R. F. Acceleration of tibial fracture-healing by non-invasive, low-intensity pulsed ultrasound. *J. Bone Joint Surg. Am.* **76**, 26–34 (1994).
8. Pilla, A. A. *et al.* Non-Invasive Low-Intensity Pulsed Ultrasound Accelerates Bone Healing in the Rabbit. *J. Orthop. Trauma* **4**, 246–253 (1990).
9. Dyson, M. & Brookes, M. Stimulation of bone repair by ultrasound. *Ultrasound Med. Biol. Suppl* **2**, 61–6 (1983).
10. Zachs, D. P. *et al.* Noninvasive ultrasound stimulation of the spleen to treat inflammatory arthritis. *Nat. Commun.* **10**, 951 (2019).
11. Tsai, C. L., Chang, W. H. & Liu, T. K. Preliminary studies of duration and intensity of ultrasonic treatments on fracture repair. *Chin. J. Physiol.* **35**, 21–6 (1992).
12. Williams, R. Production and transmission of ultrasound. *Physiotherapy* **73**, 113–116 (1987).
13. Miller, D. L. *et al.* Overview of therapeutic ultrasound applications and safety considerations. *J. Ultrasound Med.* **31**, 623–34 (2012).
14. Brugger, M. S., Stamp, M. E. M., Wixforth, A. & Westerhausen, C. Acoustotaxis - in vitro stimulation in a wound healing assay employing surface acoustic waves. *Biomater. Sci.* **4**, 1092–1099 (2016).
15. Rathgeber, A., Strobl, C., Kutschera, H.-J. & Wixforth, A. Planar microfluidics - liquid handling without walls. *J. Colloid Interface Sci.* **357**, 534–540 (2001).
16. Ding, X. *et al.* On-chip manipulation of single microparticles, cells, and organisms using surface acoustic waves. *Proc. Natl. Acad. Sci.* **109**, 11105–11109 (2012).
17. Hartmann, A. *et al.* A novel tool for dynamic cell adhesion studies-the De-Adhesion Number Investigator DANI. *Lab Chip* **14**, 542–546 (2014).
18. Collins, D. J. *et al.* Two-dimensional single-cell patterning with one cell per well driven by surface acoustic waves. *Nat. Commun.* **6**, 8686 (2015).
19. Brugger, M. S. *et al.* Orchestrating cells on a chip: Employing surface acoustic waves towards the formation of neural networks. *Phys. Rev. E* **98**, 012411 (2018).

20. Greco, G. *et al.* Surface-Acoustic-Wave (SAW)-Driven Device for Dynamic Cell Cultures. *Anal. Chem.* **90**, 7450–7457 (2018).
21. White, R. M. & Voltmer, F. W. Direct piezoelectric coupling to surface elastic waves. *Appl. Phys. Lett.* **7**, 314–316 (1965).
22. Morgan, D. *Surface Acoustic Wave Filters. Surface Acoustic Wave Filters* (Elsevier, 2007). doi:10.1016/B978-0-12-372537-0.X5000-6
23. Sritharan, K., Strobl, C. J., Schneider, M. F., Wixforth, A. & Guttenberg, Z. Acoustic mixing at low Reynold's numbers. *Appl. Phys. Lett.* **88**, 1–3 (2006).
24. Dransfeld, K. & Salzman, E. Excitation, detection, and attenuation of high-frequency elastic surface waves. *Phys. Acoust. Princ. Methods VII*, 400 (1970).
25. Strobl, F. G. *et al.* A surface acoustic wave-driven micropump for particle uptake investigation under physiological flow conditions in very small volumes. *Beilstein J. Nanotechnol.* **6**, 414–419 (2015).
26. Rambach, R. W., Skowronek, V. & Franke, T. Localization and shaping of surface acoustic waves using PDMS posts : application for particle filtering and washing †. *RSC Adv.* **4**, 60534–60542 (2014).
27. Maini, P. K., McElwain, D. L. S. & Leavesley, D. I. Traveling Wave Model to Interpret a Wound-Healing Cell Migration Assay for Human Peritoneal Mesothelial Cells. *Tissue Eng.* **10**, 475–482 (2004).
28. Doty, S. B. Morphological evidence of gap junctions between bone cells. *Calcif. Tissue Int.* **33**, 509–512 (1981).
29. Datta, S. *Surface Acoustic Wave Devices. Practise-Hall* (Prentice-Hall, 1986).
30. Foley-Nolan, D. *et al.* Low energy high frequency pulsed electromagnetic therapy for acute whiplash injuries. *Scand J Rehabil Med* **24**, 51–59 (1992).
31. Wixforth, A. Acoustically driven planar microfluidics. *Superlattices Microstruct.* **33**, 389–396 (2003).
32. Fluxion. Understanding effects of viscosity in the BioFlux system. *Tech. Note* 1–2 (2009).
33. Hancock, J. T., Desikan, R. & Neill, S. J. Role of reactive oxygen species in cell signalling pathways. *Biochem. Soc. Trans.* **29**, 345–350 (2001).
34. Duronio, R. J. & Xiong, Y. Signaling pathways that control cell proliferation. *Cold Spring Harb. Perspect. Biol.* **5**, (2013).
35. Cattin, C. J. *et al.* Mechanical control of mitotic progression in single animal cells. *Proc. Natl. Acad. Sci. U. S. A.* **112**, 11258–11263 (2015).
36. Streichan, S. J., Hoerner, C. R., Schneidt, T., Holzer, D. & Hufnagel, L. Spatial constraints control cell proliferation in tissues. *Proc. Natl. Acad. Sci. U. S. A.* **111**, 5586–5591 (2014).
37. Puliafito, A. *et al.* Collective and single cell behavior in epithelial contact inhibition. *Proc. Natl. Acad. Sci. U. S. A.* **109**, 739–744 (2012).
38. Ribeiro, C. *et al.* Enhanced proliferation of pre-osteoblastic cells by dynamic piezoelectric stimulation. *RSC Adv.* **2**, 11504–11509 (2012).
39. Esch, M. B. *et al.* Multi-cellular 3D human primary liver cell culture elevates metabolic activity under fluidic flow. *Lab Chip* **15**, 2269–2277 (2015).

40. Weder, G. *et al.* Measuring cell adhesion forces during the cell cycle by force spectroscopy. *Biointerphases* **4**, 27–34 (2009).
41. Albuquerque, M. L. C., Waters, C. M., Savla, U., Schnaper, H. W. & Flozak, A. S. Shear stress enhances human endothelial cell wound closure in vitro. *Am. J. Physiol. - Hear. Circ. Physiol.* **279**, 293–302 (2000).
42. Bednarz, J., Thalmann-Goetsch, A., Richard, G. & Engelmann, K. Influence of vascular endothelial growth factor on bovine corneal endothelial cells in a wound-healing model. *Ger. J. Ophthalmol.* **5**, 127–131 (1996).
43. Coomber, B. L. Centrosome reorientation in regenerating endothelial monolayers requires bFGF. *J. Cell. Biochem.* **52**, 289–296 (1993).
44. Reinhart, W. H. Shear-dependence of endothelial functions. *Experientia* **50**, 87–93 (1994).
45. White, C. R. & Frangos, J. A. The shear stress of it all: The cell membrane and mechanochemical transduction. *Philos. Trans. R. Soc. B Biol. Sci.* **362**, 1459–1467 (2007).
46. Dewey, C. F., Bussolari, S. R., Gimbrone, M. A. & Davies, P. F. The Dynamic Response of Vascular Endothelial Cells to Fluid Shear Stress. *J. Biomech. Eng.* **103**, 177–185 (1981).
47. Dewey, C. F. Effects of fluid flow on living vascular cells. *J. Biomech. Eng.* **106**, 31–35 (1984).
48. Dardik, A., Yamashita, A., Aziz, F., Asada, H. & Sumpio, B. E. Shear stress-stimulated endothelial cells induce smooth muscle cell chemotaxis via platelet-derived growth factor-BB and interleukin-1 α . *J. Vasc. Surg.* **41**, 321–331 (2005).
49. Hsu, S., Thakar, R., Liepmann, D. & Li, S. Effects of shear stress on endothelial cell haptotaxis on micropatterned surfaces. *Biochem. Biophys. Res. Commun.* **337**, 401–409 (2005).
50. Jo, H. *et al.* Differential effect of shear stress on extracellular signal-regulated kinase and N-terminal jun kinase in endothelial cells: G(i)2- and G β / γ - dependent signaling pathways. *J. Biol. Chem.* **272**, 1395–1401 (1997).
51. Dimmeler, S., Haendeler, J., Rippmann, V., Nehls, M. & Zeiher, A. M. Shear stress inhibits apoptosis of human endothelial cells. *FEBS Lett.* **399**, 71–74 (1996).
52. Chabanon, M. *et al.* Histological Method to Study the Effect of Shear Stress on Cell Proliferation and Tissue Morphology in a Bioreactor. *Tissue Eng. Regen. Med.* **16**, 225–235 (2019).
53. Liegibel, U. M. *et al.* Fluid shear of low magnitude increases growth and expression of TGF β 1 and adhesion molecules in human bone cells in vitro. *Exp. Clin. Endocrinol. Diabetes* **112**, 356–363 (2004).
54. Sikavitsas, V. I. *et al.* Fluid flow increases mineralized matrix deposition in three-dimensional perfusion culture of marrow stromal osteoblasts in a dose-dependent manner. *Annu. Int. Conf. IEEE Eng. Med. Biol. - Proc.* **1**, 884–885 (2002).
55. Hsu, P. P. *et al.* Effects of flow patterns on endothelial cell migration into a zone of mechanical denudation. *Biochem. Biophys. Res. Commun.* **285**, 751–759 (2001).
56. Sachs, F. & Morris, C. E. Mechanosensitive ion channels in nonspecialized cells. *Rev. Physiol. Biochem. Pharmacol.* **132**, 1–77 (1998).
57. Cox, C. D., Bavi, N. & Martinac, B. Biophysical Principles of Ion-Channel-Mediated Mechanosensory Transduction. *Cell Rep.* **29**, 1–12 (2019).
58. Demer, L. L., Wortham, C. M., Dirksen, E. R. & Sanderson, M. J. Mechanical stimulation

- induces intercellular calcium signaling in bovine aortic endothelial cells. *Am. J. Physiol. - Hear. Circ. Physiol.* **264**, 2094 - 2102 (1993).
59. Sharma, R. V. *et al.* Mechanical stimulation increases intracellular calcium concentration in nodose sensory neurons. *Neuroscience* **66**, 433–441 (1995).
 60. Ryan, M. J., Gross, K. W. & Hajduczuk, G. Calcium-dependent activation of phospholipase C by mechanical distension in renin-expressing As4.1 cells. *Am. J. Physiol. - Endocrinol. Metab.* **279**, 823–829 (2000).
 61. Pettit, E. J. & Fay, F. S. Cytosolic free calcium and the cytoskeleton in the control of leukocyte chemotaxis. *Physiol. Rev.* **78**, 949–967 (1998).
 62. Brundage, R. A., Fogarty, K. E., Tuft, R. A. & Fay, F. S. Calcium gradients underlying polarization and chemotaxis of eosinophils. *Science (80-.)*. **254**, 703–706 (1991).
 63. Clapham, D. Calcium signaling. *Cell* **131**, 1047–58 (2007).
 64. Prevarskaya, N., Skryma, R. & Shuba, Y. Calcium in tumour metastasis: New roles for known actors. *Nat. Rev. Cancer* **11**, 609–618 (2011).
 65. Howe, A. K. Cross-talk between calcium and protein kinase A in the regulation of cell migration. *Curr. Opin. Cell Biol.* **23**, 554–561 (2011).
 66. Wang, N. & Ingber, D. E. Control of cytoskeletal mechanics by extracellular matrix, cell shape, and mechanical tension. *Biophys. J.* **66**, 2181–2189 (1994).
 67. Wang, N., Butler, J. & Ingber, D. Mechanotransduction across the cell surface and through the cytoskeleton. *Science (80-.)*. **260**, 1124–1127 (1993).
 68. Matthews, B. D., Overby, D. R., Mannix, R. & Ingber, D. E. Cellular adaptation to mechanical stress: Role of integrins, Rho, cytoskeletal tension and mechanosensitive ion channels. *J. Cell Sci.* **119**, 508–518 (2006).
 69. Jötten, A. M. *et al.* Correlation of in vitro cell adhesion, local shear flow and cell density. *RSC Adv.* **9**, 543–551 (2019).
 70. Voss, M. *et al.* Shedding of glycan-modifying enzymes by signal peptide peptidase-like 3 (SPPL3) regulates cellular N-glycosylation. *EMBO J.* **33**, 2890–2905 (2014).
 71. Kuhn, P.-H. *et al.* Secretome Analysis Identifies Novel Signal Peptide Peptidase-Like 3 (SPPL3) Substrates and Reveals a Role of SPPL3 in Multiple Golgi Glycosylation Pathways. *Mol. Cell. Proteomics* **14**, 1584–1598 (2015).
 72. Paluch, E. K. *et al.* Mechanotransduction: use the force(s). *BMC Biol.* **13**, 47 (2015).
 73. Jin, H. *et al.* Flexible surface acoustic wave resonators built on disposable plastic film for electronics and lab-on-a-chip applications. *Sci. Rep.* **3**, 2140 (2013).
 74. Beck, K. *et al.* Inductively coupled surface acoustic wave device for sensor application. *IEEE Trans. Ultrason. Ferroelectr. Freq. Control* **45**, 1140–1144 (1998).



Supplementary Information for

Vibration enhanced cell growth induced by surface acoustic waves as in vitro wound healing model

Manuel S. Brugger, Kathrin Baumgartner, Sophie. C. F. Mauritz, Stefan C. Gerlach, Florian Röder, Christine Schlosser, Regina Fluhrer, Achim Wixforth and Christoph Westerhausen

Christoph Westerhausen

Email: christoph.westerhausen@gmail.com

This PDF file includes:

Supplementary text
Figures S1 to S5
Legends for Movies S1 to S3
SI References

Other supplementary materials for this manuscript include the following:

Movies S1 to S3

Supplementary Information Text

Methods and Materials

SAW-Chip

The key interest of our study lies in the observation that cell growth and cell migration are positively assisted by a SAW-based ultrasonic cell stimulation. The major advantage here is the fact that SAW can be excited on the spot where cells grow and proliferate. For this purpose, SAW are generated on a small piezoelectric chip where micron sized metal electrodes, so-called Interdigital Transducers (IDT) are supplied with an rf signal which then is effectively converted into a well-defined, piezoacoustic surface wave, just like in the above mentioned rf filters in mobile phones. Depending on the desired wave mode, the substrate is chosen to be either LiNbO₃ in Y-cut with the crystal axes rotated around the X-axis by 128° (128° rot Y-cut) (LB) or LiTaO₃ 40° rot X-Y-cut (LT)(1). The IDT is deposited on top of the substrate by using standard lithography technique. It consists of two multi-finger electrodes (Ti-Au-Ti, $d_{Ti} = 5$ nm, $d_{Au} = 50$ nm) and adjusted to the radio frequency (rf)-systems impedance of $Z = 50$ Ohm, as first described by White and Voltmer(2). The width of the IDT aperture is $W = 650$ μ m and $W = 600$ μ m, respectively. The periodicity of the electrodes in our studies is $a = 25$ μ m and $a = 50$ μ m, respectively which converts to $\lambda_{SAW} = 25$ μ m and $\lambda_{SAW} = 50$ μ m. λ_{SAW} and the SAW velocity of the substrate, results in the resonant SAW excitation frequency $f = c/\lambda_{SAW}$. For example, the SAW velocity of LiNbO₃, $c_{LB} = 3980$ m/s, and $\lambda_{SAW} = 25$ μ m results in $f_{res} = 159$ MHz. To ensure biocompatibility and to protect the micron sized electrodes, the whole SAW chip except for the contact pads is covered with a 200 nm thick SiO₂ layer. This layer was deposited by thermal evaporation. By feeding a rf-signal of power P_{IN} and frequency f_{res} to the IDT, a spatio temporal, quasi monochromatic and coherently propagating surface deformation, the surface acoustic wave, is generated due to the inverse piezoelectric effect. Dependent on the substrate, cut and transducer design the wave is either a Rayleigh SAW with longitudinal and transversal components for LB or a horizontally polarized love wave for LT(1).

For each experiment and to assess the actual acoustic performance and resonance frequency of the chip, the frequency response is determined beforehand with a network analyzer (NWA) (ZVR, Rhode & Schwarz GmbH & Co. KG., Munich, Germany). The measured frequency-dependent quadripolar reflection coefficient S_{11} is then used to determine the actual resonance frequency and the transconductance of the chip. Typically, for unloaded chips and for the minimal reflection it holds $S_{11} < -18$ dB. The rf-power fed into the IDT is measured in mW or dBm, according to the following relation:

$$P_{IN}(\text{dBm}) = 10 \log_{10} \left(\frac{P(W)}{1 \text{ mW}} \right) \quad @ Z = 50 \text{ Ohm}.$$

The simple symmetric IDT design used in this study operates bidirectionally, i.e., it launches SAW in both directions. The acoustic energy P_{SAW} interacting with the cell sample can then be estimated from the minimal reflection value S_{11} and a typical insertion loss of $IL \approx -3$ dB. It turns out that P_{SAW} of the propagating wave in our case and for a free substrate surface is $P_{SAW} \approx \frac{1}{4} P_{IN}$. If the thickness of any surface covering material is not negligible as compared to the SAW wavelengths, the SAW is dissipatively attenuated which causes, e.g., the SAW-induced acoustic streaming(3). This out-of-plane-attenuation leads to a 1/e-decay length of the SAW-intensity in propagation-direction which in water turns out to be $l_{opX}^{Calc} = 12.5 * \lambda_{SAW} = 331$ μ m (4). Considering the 1/e-decay length and the aperture width W , the SAW-intensity I_{SAW} acting upon the cells is approximately(4):

$$I_{SAW} = P_{SAW} \frac{\left(1 - \frac{1}{e}\right)}{W * l_{opX}^{Calc}} \approx 80 \frac{\text{mW}}{\text{cm}^2} \quad \text{for } P_{IN} = 1 \text{ mW} \quad \text{and} \quad I_{SAW} \approx 1 \frac{\text{W}}{\text{cm}^2} \quad \text{for } P_{IN} = 13.6 \text{ mW}.$$

For a more detailed assessment of the SAW-intensities, see our previous work(5). For the rf-signal supply of the IDT, a conventional generator (SML-01, Rhode & Schwarz GmbH & Co. KG., Munich, Germany) and a power amplifier (AMP590033H-T, Becker Nachrichtentechnik GmbH, Asbach, Germany) are used.

Cells and cell culturing

This study comprised two cell lines, 'Madine-Darby Canine Kidney' (MDCK-II) and human osteosarcoma 'sarcoma osteogenic' (SaOs-2). The epithelial cell line MDCK-II (ECACC Cat.No.: 00062107) and the SaOs-2 (ECACC Cat.No.: 89050205) were obtained from Sigma Aldrich, Germany. While the MDCK-II cell line provides a perfect model to study epithelia as they have well defined cell junctions, rapid growth rate and a clear apico-basolateral polarity, SaOs-2 cells are suitable to study osteoblastic properties. Additional information on the cell properties can be found elsewhere(6, 7). Both lines were cultured as an adhesive monolayer in the medium recommended by ECACC in Nunc™ cell culture flasks (ThermoFisher Scientific, MA, USA) and in a saturated atmosphere with 5 % CO₂ at $T = 37^{\circ}\text{C}$. The media (SaOs-2: HAMS F12; MDCK-II: MEM Earle's; Biochrom GmbH, Berlin, Germany) were supplemented with 10 % fetal bovine serum (FBS Superior) and 0.2 % Primocin (InvivoGen, Toulouse, France) for HAMS F12 and 1 % Pen/Strep (Biochrom GmbH, Berlin, Germany) for MEM Earle's. Cell passaging followed the standard trypsinization procedure using 1 ml Trypsin/EDTA (SaOs-2: 0.05 %, MDCK-II: 0.25 %) solution and PBS (w/o Ca²⁺, w/o Mg²⁺) (Biochrom GmbH, Berlin, Germany). T-Rex™-293 (HEK293) (Invitrogen, Hennigsdorf, Germany) were cultured in DMEM with Glutamax (Invitrogen, Hennigsdorf, Germany) supplemented with 10% fetal calf serum (Sigma), 1% penicillin/streptomycin (Gibco) and 5µg/ml Blasticidin (Invitrogen, Hennigsdorf, Germany). At least 48h before start of the experiment cells were cultured in antibiotic free medium. Cell density was adjusted to 80.000 cells per 100 µl.

Wound healing assay

If not stated otherwise, for each of the following experiments including cells, a wound healing assay was performed while measuring different cellular parameters. The wound healing assay provides the possibility to monitor the progressive cell migration of two opposing confluent cell layers into a cell-free area. To obtain standardized starting conditions such as confluency, cell density or the width of the cell-free area, a commercially available silicon chamber assay was used. This so called culture insert (CI) (Ibidi® GmbH, Martinsried, Germany; width 500 µm +/- 50 µm) consists of two chambers with one adhesive side as illustrated in Fig. 1. a-1). Upon confluency, an artificial 'wound' in a confluent cell layer can be created by its removal. After a short delay, cells at the edges of the confluent layers subsequently start to migrate into the empty gap at a constant speed(8).

The experimental setup

The above described SAW-chip was mounted on an in-house made sample holder providing the rf-micro strip lines and connectors to the generator. Contacts between the chip and the board were made by a silver conducting paste (Acheson Silver DAG 1415M, Acheson Industries Inc., MI, USA). To hold the culture nutrient and to house the cells, a polydimethylsiloxane (PDMS) chamber ($V = 3$ ml) (Sylgard 184 Silicone Elastomer, Dow Corning, Germany; m/m ratio 10:1) was placed on top of the SAW-chip. To avoid leakage between chamber and SAW-chip the contact surfaces were coated with a thin layer of highly viscous silicon grease (Baysilicon-Paste, GE Bayer Silicones, Leverkusen, Germany). To maintain sterility of this reusable system, the whole setup was autoclaved at $T = 134^{\circ}\text{C}$ prior to each experiment and exposed to UV-illumination. Under a microscope, the disposable CI was then carefully placed with its gap oriented parallel to the IDT aperture and about $d = 50$ µm away from the IDT. Then, 80.000 cells in 100 µl cell suspension were seeded into each of the two chambers of the CI. Upon cell adhesion, the entire chamber was filled with $V = 1$ ml of nutrient. Subsequently, the cells grew for 24 hours to reach confluency. After the removal of the CI, the cell layers were washed three times with 0.5 ml PBS and refilled with $V = 3$ ml of fresh nutrient. For the live cell imaging experiments, up to four chips were placed in parallel on the motorized microscope stage (MAC 5000, Ludl Electronic Products Ltd., NY, USA) and connected to a rf-generator. To sustain optimal growth conditions (saturated atmosphere with 5 % CO₂ at $T = 37^{\circ}\text{C}$) a microscope incubator (ibidi Heating & Gas Incubation System, Munich, Germany) was used. The migration process into the cell-free area was then observed with a microscope (Zeiss Axiovert 200M, Göttingen, Germany) and phase contrast images at multiple positions were taken automatically every five minutes with a 10 x objective.

Measuring intracellular parameters

In order to understand the cellular response and the corresponding biochemical processes behind the SAW-stimulation, different accessible cell parameters are measured. In this study, we determined the production of ROS, the proliferation rate of SAW-stimulated cells and their corresponding internal and external reference. To ensure consistent environmental conditions, the parameters were measured in the framework of a standard wound healing assay. After the removal of the CI, the cells were irradiated by SAW at different power levels while being cultivated in 5 % CO₂ at 37°C (HERAcell® 150 CO₂ Incubator, ThermoFisher Scientific Massachusetts, USA). Depending on the measurand, the measurement protocol was performed during or directly after the treatment as being specified in the following. To detect the cell nucleoli independent from the respective state and size, the DNA binding fluorescent dye Hoechst 33342 (NucBlue® Live ReadyProbes® Reagent, Cat. No.: R37605 - ThermoFisher Scientific, Massachusetts, USA) was used (ex./em.: ~360/460 nm). Subsequent to the different staining protocols, the samples were analyzed using the previously described microscope at 10 x magnification. Phase contrast and fluorescence images for DAPI (Ex. 350/50 / Em. 460/50 (AHF-F46-000-DAPI, AHF Analysentechnik AG, Tübingen, Germany)) and FITC (Ex. 475/35 / Em. 530/43 (MDF-FITC, Thorlabs Inc, Newton, NJ, USA)) were taken for a large area around the aperture.

ROS: For the detection of ROS, CellROX® Green Reagent (Cat. No.: C10444 - ThermoFisher Scientific, Massachusetts, USA) was used. This fluorogenic probe is cell-permeant and weakly fluorescent while residing in reduced state. Upon oxidation by ROS, and subsequent binding to DNA, the probe exhibits a bright, green and photostable fluorescence (ex./em.: ~485/520 nm). Next to the SAW-stimulated samples, untreated 'low' controls as well as 'high' controls are prepared for each test row. Cells in the 'high' control were treated with 100 µM of menadione (Cat. No.: M2518 – Sigma Aldrich, St. Louis, MO, USA) for 1-hour prior the end of SAW-irradiation. After 24 hours of SAW-irradiation, $V = 250\ \mu\text{l}$ of the nutrient supernatant was removed and 40 µM CellROX Green as well as $V = 15\ \mu\text{l}$ NucBlue were added and thoroughly mixed. The remaining nutrient was discarded and replaced by the mixture. After 30 minutes of incubation at 37°C and 5% CO₂ the mixture was discarded and the cell layer was washed three times with $V = 1\ \text{ml}$ PBS and refilled with $V = 1\ \text{ml}$ fresh nutrient.

Proliferation: To identify proliferating cells in the monolayer the proliferation assay Click-iT™ EdU Cell Proliferation Kit (Cat. No.: C10337 – ThermoFisher Scientific, MA, USA) was used. Here, the modified thymidine analogue EdU is incorporated to freshly synthesized DNA and subsequently labeled with a green fluorescence dye. For detailed information, see the manufacturer's protocol(9). Following the removal of the CI, $V = 1\ \text{ml}$ of a 20 µM EdU-nutrient solution is added to the culture and the SAW is turned on for 27 hours. The next steps are performed as suggested by the manufacturer.

Data analysis

Wound healing Assays:

The phase contrast images were stitched by a home-made software. The cell-free area was analyzed semi-automatically using the modified ImageJ macro "MRI-Wound healing tool" (http://dev.mri.cnrs.fr/projects/imagej-macros/wiki/Wound_Healing_Tool) and, if necessary corrected manually. In Fig. 1 b) a chronological sequence of a typical experiment at different time points is shown. The cell fronts continuously invade the red-labelled cell-free area over time. Determined by the IDT layout, the width of the sound path is strictly limited to the size of the aperture(10). Therefore, only cells in front and rear of the aperture are directly stimulated by SAW. The cell-free area in this region is called *aperture* in the following. The length of the gap is many times larger than the aperture and its stimulated section. This allows comparison of the SAW-irradiated cells with an internal and natural reference. As shown in the inset of Fig. 1. c) the internal references indicated in green and blue are located next to the wiring. At these positions, the SAW does not interact with the cells. Yet, cells grow under identical conditions (i.e. nutrient supply, temperature, cell density, current cell cycle, viability etc.) as the sample in front of the aperture on the same chip.

In a wound healing assay, a typical parameter is the 'surface area migration rate A_{mig} ', which describes the speed of cell migration and growth into the free space. For the evaluation of A_{mig} the cell-free area is determined for every region of interest in $\Delta t = 1.25$ h intervals and plotted as function of the elapsed time as shown in Fig. 1. c). The cell-free area $F(t)$ was normalized to the cell-free area $F(0)$ at the beginning of each experiment. The measured $F(t)$ can be approximated by a linear fit. To exclude artefacts in the beginning and at the end of the healing process, only values in the interval $0.8 < F(t) < 0.2$ are taken into account. The slope of the linear fit A_{mig} with the unit area loss in percent per hour. To compare the results and to avoid culture dependent influences, the aperture $A_{\text{mig, aperture}}$ is divided by the mean of the internal references $A_{\text{mig, int. ref.}}$ shown in Fig. 2 d). This ratio is defined as stimulation efficacy $E := A_{\text{mig, aperture}}/A_{\text{mig, int. ref.}}$. For each power four separate experiments are performed if not indicated otherwise.

To identify the cell migration over time in one image, grayscale-coded images as shown in Fig. 1 d) are created. One image is the superimposed composition to the complete sequence of one sample. Dependent on the elapsed time, the gray value of the area becomes brighter. We interpret this finding that an early coverage of an area with cells results in a darker color. To maintain a high-quality content of the scientific data, the cell layer in the analyzed region must meet some specific demands like confluency, cell density and viability. As exemplary being shown in Fig. 1 d-3) the right part of the cell layer was not completely confluent as compared to the one in Fig. 1 d-1) - 2). Therefore, only the left part was considered for the internal reference. However, this concerns only a small fraction of all samples.

Fluorescence images:

To evaluate the fluorescence images, the data were analyzed using a self-developed software in MATLAB (MathWorks, Natick, MA, USA). Important MATLAB-specific code commands and parameters are being mentioned in brackets. For evaluation, the recorded 12-bit grayscale images at one position in the DAPI and FITC channel are considered. The phase contrast images were used to verify the cell layer quality qualitatively in the beginning. Next, if necessary, any possible non-uniform illumination in the fluorescence images was rectified using a background image or the mean of all images which had been blurred before. The next steps are dependent on the measurand and are explained briefly:

ROS: The CellROX® Green reagent is a DNA dye and, thus, primarily localizes to the nucleus and mitochondria(11). Detection of the nucleus in the DAPI image is the first step. To accurately distinguish all cells from the background, the images were analyzed using the machine learning algorithm *ilastik: Interactive learning and segmentation toolkit*(12). After removing small objects (*bwareaopen*), the objects were filtered depending on size and subsequently dilated (*imdilate, factor: 2*). Cell clusters are then partitioned by using the watershed-method. This allows to mask the complete area of the nucleus and the one in its close vicinity. The objects' data are then used to calculate the mean gray value of all pixels of one object in the FITC-image. The mean values and their corresponding center coordinates are saved and exported and analyzed depending on the region. The ROS concentration in the 'high' control, however, can vary quite strongly. To only take the maximum concentration for the 'high' control into account, the mean value of the upper five percent of the complete 'high' control sample is evaluated. To avoid errors from the actual condition of the cells, the 'high' control is calculated from the mean of all performed samples. Yet, the related low control is determined separately for each experiment.

Stress level – ROS

Estimating negative effects induced by high SAW-intensities by measuring the intracellular concentration of reactive oxygen species (ROS). SI-Fig. 5 a), a typical image of the intracellular stress of SAW-stimulated cells at a power level of $P_{\text{IN}} = 64$ mW is shown. In Fig. 5 b) – d) a zoom in of the region close to the IDT is visible. The quality of the cell layer and possible morphological changes are verified for each sample using phase contrast imaging (Fig. 5 b)). The position information of the nuclei in Fig. 5 c) is used to determine the cellular stress level in Fig. 5 d). To investigate ROS as a function of the applied power level P_{IN} , selected regions indicated by colored rectangles with $\Delta x = 300$ μm and $\Delta y = 650$ μm are evaluated in Fig. 5 a). Fig. 5 e) displays the power-dependent ROS concentration in the evaluated areas. At very high SAW-

powers ($P_{IN} = 128 \text{ mW}$), some cells start to become ripped off the substrate inter alia caused by the high shear stress induced by the acoustic streaming as shown in Fig. 5 f).

Proliferation: The ratio of the number of proliferated cells and the total number of cells was evaluated. By using two DNA-binding dyes (Hoechst 33342 and EdU binding Alexa Fluor® 488), both probes likely locate in the same region having identical surface areas. This allows us to directly compare the total area of labeled cells in the DAPI and FITC channel. Due to the overlapping excitation and emission spectra of the dyes, a fluorescence resonance energy transfer (FRET) occurs, leading to a slightly darker intensity signal of proliferated cells in the DAPI channel compared to the non-proliferated cells. Here, the machine learning algorithm *ilastik* clearly shows its efficiency by detecting all cell nuclei. The binary images of the DAPI and FITC are then separated in the regions of interest (aperture, internal reference). The median size of the cell nuclei is evaluated for each section by using 'Analyze Particles' in ImageJ. Then, the total amount of white pixels in the DAPI and FITC channel is divided by their corresponding median cell size in order to assess the number of cells in the images. The ratio of cell nuclei in the FITC-channel through the total amount of cells in DAPI-channel is the ratio of proliferating cells in the region. The difference in the proliferation is measured by the statistical change in the number of proliferated cells in the sound path compared to a reference.

The data were statistically analyzed using the Student's t-test (paired, verified by the Levene-test) using the software Microsoft Office - Excel 2016 (Microsoft, Redmond, WA, USA). Results where $p < 0,05$ was obtained are statistically significant.

Results and Discussion

Variation of coverage speed

We analyzed the "wound healing speed" along the device, more precise along the cell free area entitled the artificial wound. For this analysis, we analyzed the recorded area in lines with the width of 1000 px. This results in 7 positions along the device. For these stripes we analyzed the migration velocity of the cell front to determine, the point in time when the migration of the cell front stops. The reciprocal value of this time we define as the gap closing speed. The stripes 2 and 7 here mainly cover the regions that we used as internal reference for the data shown in Fig. 2 and 3. Thus, we normalized the gap closure speed to the mean value of these two stripes. The result (SI-Fig. 2) and the according text from the SI below.

The results show that only the region in front of the aperture shows a significant increased gap closure speed ($p < 5\%$). However, the direct neighbors show increased values as well ($p \approx 10\%$ and $p \approx 36\%$). These might be a consequence of some bystander effect that can not be avoided in such a system. This analysis supports our argumentation in the manuscript.

Estimate the electrical stimulation efficacy

In order to assess the stimulation contribution of the SAWs electrical component, we performed an additional reference measurement. Here, the electrical field is weakened by shortening the lateral component with a 10 nm thick Titanium layer. Ensuring biocompatibility, the Titanium layer is covered with a 200 nm thick SiO_2 layer. The SAW-chip consisted of the material LB with an IDT ($\lambda_{\text{SAW}} = 25 \mu\text{m}$, $W = 650 \mu\text{m}$) on top. The experiment is performed using SaOs-2 cells.

Estimate the streaming effect

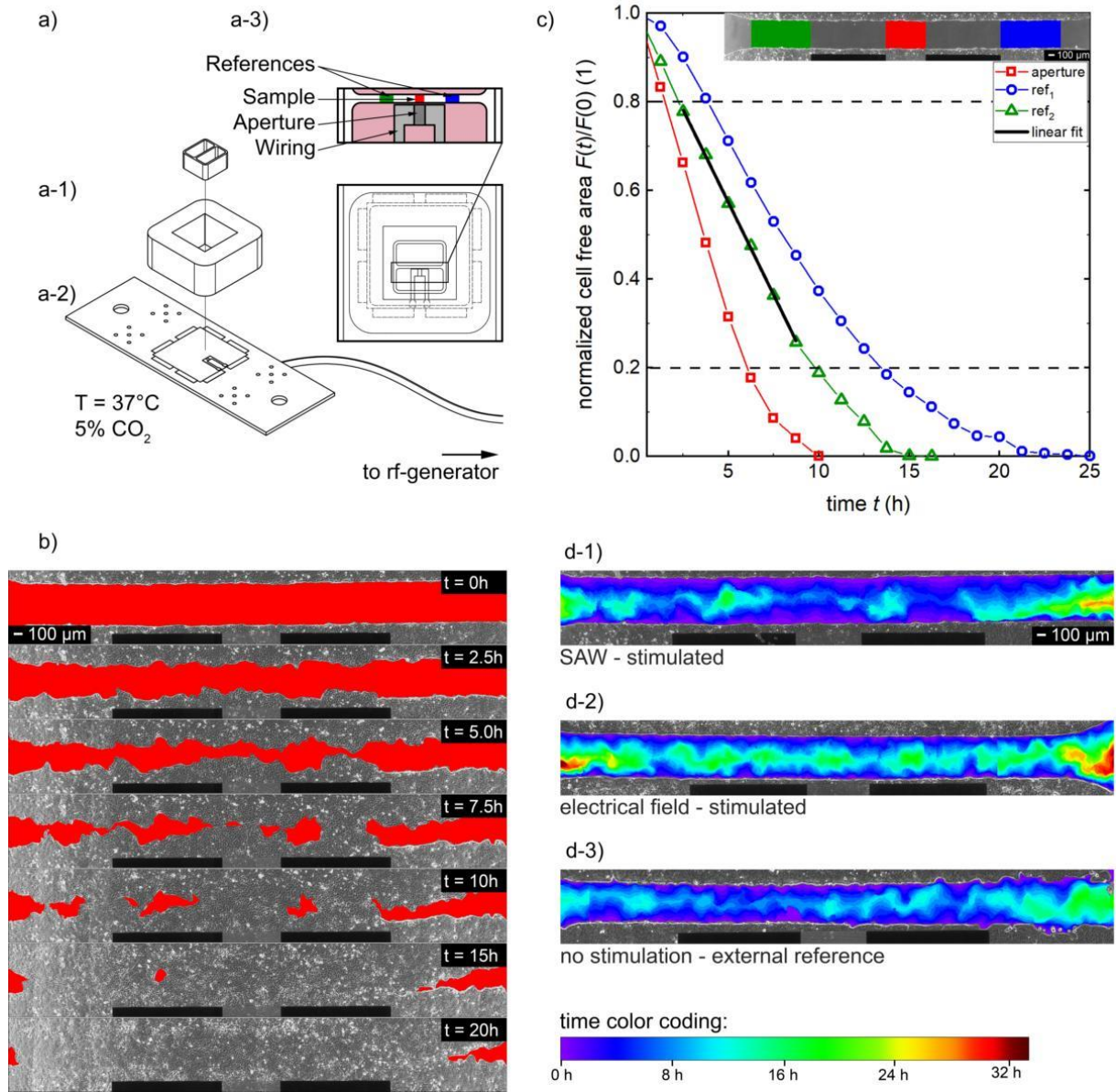
As cells can be influenced by streaming effects we investigated the cell growth of SaOs-2 cells in stirred media. In this experiment, the IDT is placed aside the artificial gap inducing a streaming by the Leaky-SAW. We used the material LB, a wavelength of $\lambda_{\text{SAW}} = 25 \mu\text{m}$ and applied a rf-power of $P_{IN} = 4 \text{ mW}$, where we observed a significant increase in the efficacy E in the previous experiments. The SAW-Chip design and the positioning of the CI is displayed in SI Fig. 4 The cell growth in the stirred media is compared to an external reference with a static media. The surface coverage rate A_{mig} is evaluated along the complete gap for both the sample and the external reference. The

determined efficacy E with $E := A_{\text{mig, sample}} / A_{\text{mig, ext. ref}}$ is calculated on the basis of three separate test runs.

Stress level – ROS

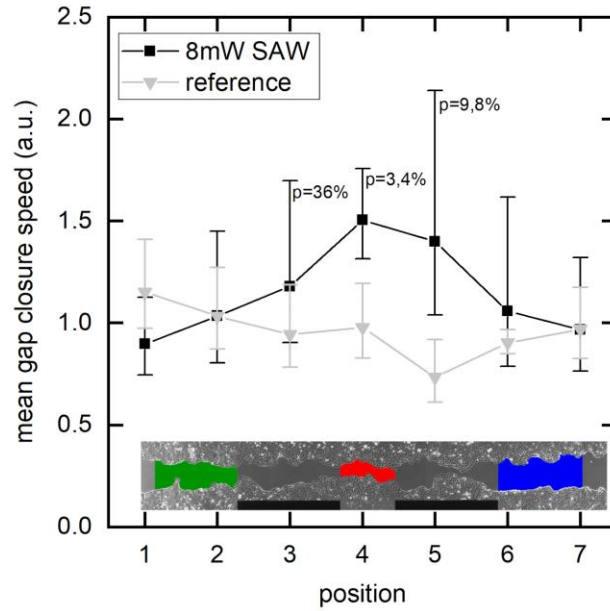
Estimating negative effects induced by high SAW-intensities by measuring the intracellular concentration of reactive oxygen species (ROS). SI-Fig. 5 a), a typical image of the intracellular stress of SAW-stimulated cells at a power level of $P_{\text{IN}} = 64 \text{ mW}$ is shown. In Fig. 5 b) – d) a zoom in of the region close to the IDT is visible. The quality of the cell layer and possible morphological changes are verified for each sample using phase contrast imaging (Fig. 5 b)). The position information of the nuclei in Fig. 5 c) is used to determine the cellular stress level in Fig. 5 d). To investigate ROS as a function of the applied power level P_{IN} , selected regions indicated by colored rectangles with $\Delta x = 300 \text{ }\mu\text{m}$ and $\Delta y = 650 \text{ }\mu\text{m}$ are evaluated in Fig. 5 a). Fig. 5 e) displays the power-dependent ROS concentration in the evaluated areas. At very high SAW-powers ($P_{\text{IN}} = 128 \text{ mW}$), some cells start to become ripped off the substrate inter alia caused by the high shear stress induced by the acoustic streaming as shown in Fig. 5 f).

Fig. S1.



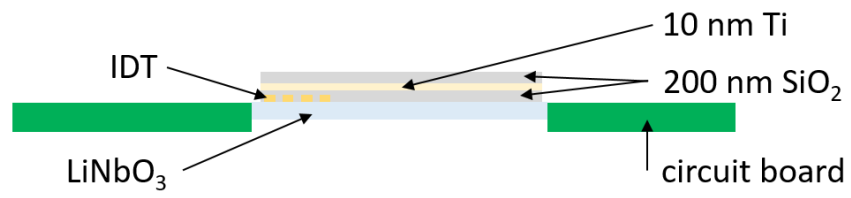
Sketch of the experimental setup and concept of the data analysis. a) Technical drawing of the setup. A culture insert was used to produce a standardized artificial wound in a confluent cell layer (pink) of MDCK-II cells in front of the IDT aperture. b) Time sequenced images of the progressive cell migration of MDCK-II cells into the cell-free area (red). c) Time dependent shrinkage of the normalized cell-free area in the regions of interest (red: stimulated section, green/blue: internal reference). The section between $0.8 < F(t)/F(0) < 0.2$ is approximated by a linear fit. The slope gives the surface area migration rate A_{mig} . d) Superimposed snapshots of the cell fronts of single experiments at different time steps for a time dependent color coded migration progress. d-1)-2) Analyzable samples. d-3) Cell layer quality of the right area does not meet the requirements

Fig. S2.



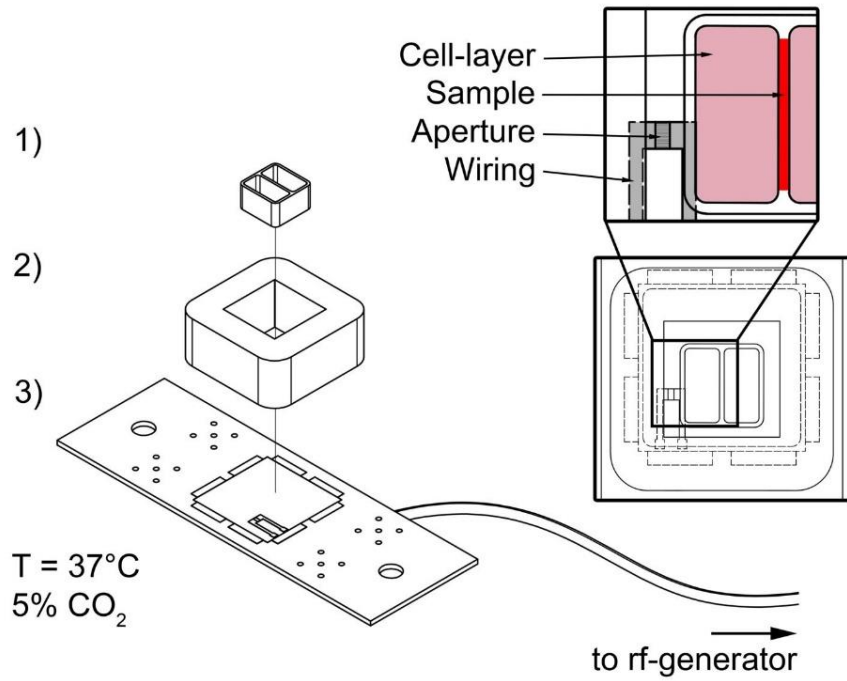
Mean gap closure speed as function of position along the cell free area for MDCKII cells. Position 4 covers the region in front of the aperture, while the internal references are located at about position 2 and 7. Black squares: mean value of $n = 4$ measurements at a power level of $P_{IN}=8$ mW. Grey triangles: mean value of $n = 4$ reference measurements without applied SAW. For the positions 3, 4 and 5 p-values are obtained by a two-sided t-test. Here the results of each position is tested against the results at the internal reference positions 2 and 7.

Fig. S3.



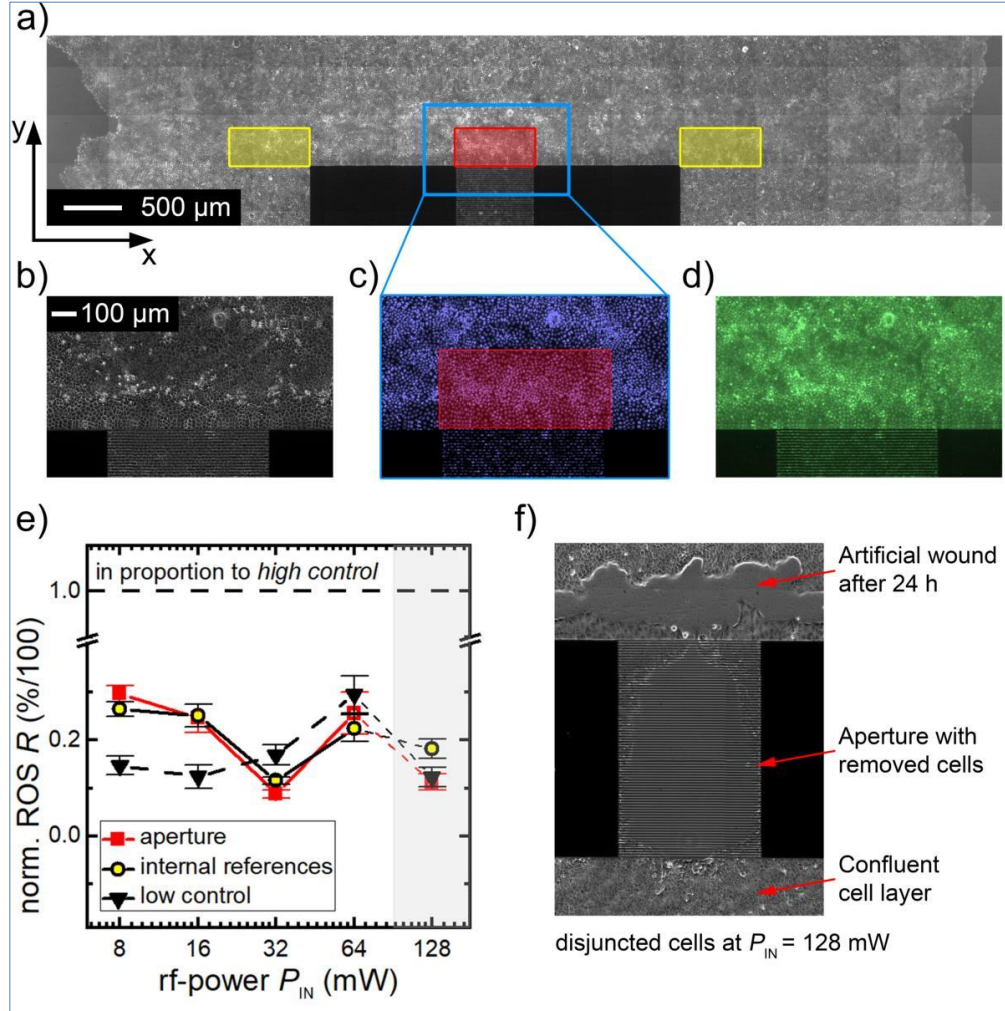
Alternative SAW-chip design to weaken the strength of the electrical field. Using a 10 nm thick Titanium layer on top of the first SiO_2 layer, the lateral electrical field is shortened. SaOs-2 cells were growing on the second SiO_2 layer.

Fig. S4.



Technical drawing of the experimental setup in exploded- (left) and top-view (right). A culture insert (1)) was used to produce a standardized artificial wound in aside the IDT aperture on a SAW-Chip (3)). The PDMS-chamber (3)) hold the nutrient. The complete gap (red) is used to determine the surface coverage rate A_{mig} .

Fig. S5.



Characterizing the SAW-induced increase of ROS in cells. a) Phase contrast image of the cell layer with evaluated regions marked by colored rectangles (red: aperture, yellow: internal reference). b)-d) Images taken for each measurement: b) phase contrast image, c) cellular nuclei d) ROS in cells. e) Comparison of the ROS concentration relative to the high control. f) Phase contrast image at $P_{\text{IN}} = 21 \text{ dBm}$.

Movie S1 (separate file). SAW, $f=164$ MHz, PIN = 16 mW, $\lambda_{SAW} = 25$ μ m, MDCK-II

Movie S2 (separate file). E-field, $f=100$ MHz, PIN = 16 mW, $\lambda_{SAW} = 25$ μ m, MDCK-II

Movie S3 (separate file). SAW, $f=164$ MHz, PIN = 16 mW, $\lambda_{SAW} = 25$ μ m, MDCK-II, top: phase contrast image with cell free area labeled in red, bottom: superimposed snapshots of the cell fronts at different time steps with a time dependent color-coded migration progress

SI References

1. D. Morgan, *Surface Acoustic Wave Filters, 2nd Edition*, Second (Academic Press, 2007).
2. R. M. White, F. W. Voltmer, Direct piezoelectric coupling to surface elastic waves. *Appl. Phys. Lett.* **7**, 314–316 (1965).
3. K. Sriharan, C. J. Strobl, M. F. Schneider, A. Wixforth, Z. Guttenberg, Acoustic mixing at low Reynold's numbers. *Appl. Phys. Lett.* **88**, 1–3 (2006).
4. K. Dransfeld, E. Salzman, Excitation, detection, and attenuation of high-frequency elastic surface waves. *Phys. Acoust. Princ. Methods VII*, 400 (1970).
5. M. S. Brugger, M. E. M. Stamp, A. Wixforth, C. Westerhausen, Acoustotaxis - in vitro stimulation in a wound healing assay employing surface acoustic waves. *Biomater. Sci.* **4**, 1092–1099 (2016).
6. J. D. Dukes, P. Whitley, A. D. Chalmers, The MDCK variety pack: choosing the right strain. *BMC Cell Biol.* **12**, 43 (2011).
7. S. B. Rodan, *et al.*, Characterization of a Human Osteosarcoma Cell Line (Saos-2) with Osteoblastic Properties. *Cancer Res.* **47**, 4961–4966 (1987).
8. P. K. Maini, D. L. S. McElwain, D. Leavesley, Travelling waves in a wound healing assay. *Appl. Math. Lett.* **17**, 575–580 (2004).
9. T. Scientific, Click-iT EdU Imaging Kits (Manual). *Life Technol. Corp.*, 1–8 (2011).
10. T. Frommelt, "Mischen und Sortieren mit SAW-Fluidik in Simulation und Experiment," Augsburg. (2007).
11. T. Scientific, CellROX® Oxidative Stress Reagents. *Life Technol. Corp.*, 1–6 (2012).
12. C. Sommer, C. Straehle, U. Kothe, F. A. Hamprecht, Ilastik: Interactive learning and segmentation toolkit in 2011 *IEEE International Symposium on Biomedical Imaging: From Nano to Macro*, (IEEE, 2011), pp. 230–233.